Non-peer reviewed Preprint submitted to EarthArXiv

Title: **Current deformation in Hispaniola from InSAR–derived surface velocities**

Authors: Bryan Raimbault, Romain Jolivet, Éric Calais, Steeve J. Symithe and Christian Emmanuel

Affiliation:
Centre National d'Etudes Spatiales, CNES, Toulouse, France
École normale supérieure, Department of Geosciences, Université PSL, CNRS, Paris, France
Institut Universitaire de France, Paris, France
Université d'État d'Haïti, Faculté des Sciences, URGéo, Port-au-Prince, Haïti

Current deformation in Hispaniola from InSAR–derived surface velocities

B. Raimbault[1,2], R. Jolivet[2,3], E. Calais[2], S. Symithe[4], C. Emmanuel[2]

[1]Centre National d'Etudes Spatiales, CNES, Toulouse, France
[2]École normale supérieure, Department of Geosciences, Université PSL, CNRS, Paris, France
[3]Institut Universitaire de France, Paris, France
[4]Université d'État d'Haïti, Faculté des Sciences, URGéo, Port-au-Prince, Haïti

Key Points:

- Complete 3D velocity map of Hispaniola from SAR persistent scatterers interferometry
- Strain accumulation on the Enriquillo, Jérémie-Malpasse, and Septentrional faults
- Enriquillo fits a single locked fault model and the Septentrional likely involves faults
- Strain in SE Hispaniola modeled by a reverse fault indicates a significant hazard source

Corresponding author: Bryan Raimbault, `bryan.raimbault@cnes.fr`

Abstract

The oblique convergence between the Caribbean and North American plates is accommodated, in Hispaniola, by left-lateral strike-slip on two major left–lateral fault systems and by intra-arc shortening. We apply a Persistent Scatterer Interferometry (PSInSAR) approach to Sentinel-1 data using six tracks acquired between 2016 and 2023 to generate time series of interseismic velocities over the entire island. We merge the resulting ascending and descending tracks with GNSS–derived velocities to determine a spatially-continuous 3D velocity field that documents deformation gradients across large fault systems. The Enriquillo fault fits a single locked–fault model, while the Septentrional one likely involves several sub–faults. Strain in southeastern Haiti and the southwestern Dominican Republic is well modeled by the Jérémie-Malpasse-Bahoruco oblique reverse fault-system , which represents a significant, but overlooked, regional hazard source.

1 Introduction

Current deformation in the Caribbean region combines the frontal subduction of the Atlantic oceanic lithosphere beneath the Lesser Antilles with two zones of transpressive deformation along the northern and southern boundaries of the Caribbean plate (e.g., Burke, 1988). While the North American and South American plates show little relative movement (Patriat et al., 2011), the Caribbean plate moves eastward relative to both at a rate of 18–20 mm/yr (DeMets et al., 2000; Symithe et al., 2015). In the northern Caribbean (Figure 1), this relative motion combines convergence and strike-slip, accommodated primarily for the former by the Puerto Rico – North Hispaniola subduction, and by the Oriente – Septentrional and Enriquillo Plantain-Garden fault systems for the latter (Mann et al., 1995, 2002; Calais et al., 1992).

Slip and strain rates across the Caribbean-North America plate boundary in Hispaniola have so far been obtained mainly by inverting horizontal velocities derived from Global Navigation Satellite System (GNSS) measurements using so–called "block models" (Meade & Loveless, 2009; McCaffrey, 2013). Such models assume that geodetic velocities combine the rotation of rigid elastic blocks and strain buildup on the locked – or partially locked – block–bounding faults. This allows them to provide fault slip rates – slip deficit rates in fact – which are directly relevant to regional kinematics and hazard estimation. Such models, however, rely on predefined fault geometries, which are not always well-known. They are also limited by the number and density of GNSS measure-

ments, which are often non-uniformly spaced and may not properly sample the actual velocity gradients. Nevertheless, over the years kinematic block models constrained by GNSS measurements have provided slip deficit rates for the Enriquillo and Septentrional left–lateral strike–slip faults, as well as for the Muertos and Puerto Rico–North Hispaniola convergence systems (e.g., Manaker et al., 2008; Benford et al., 2012; Symithe et al., 2015).

Slip deficit on these major fault systems is also attested by slip released during large earthquakes, as shown by the ∼500 year–long historical record available (Fig. 1; Scherer, 1912; Bakun et al., 2012; Martin & Hough, 2022; Hough et al., 2023). In the recent times, two large events struck the Southern Peninsula of Haiti in 2010 (Mw7.0) and 2021 (Mw7.2), potentially releasing some of the slip deficit accumulated on the Enriquillo fault since the 18th century. However, source models derived from aftershock distributions and geodetic inversions show that both events ruptured unmapped, blind transpressional faults oblique to the main Enriquillo fault (Hayes et al., 2010; Calais et al., 2010; Douilly et al., 2013; Symithe et al., 2013; Raimbault et al., 2023; Douilly et al., 2023), indicating a complexity level in the fault system that is yet to be fully described and understood. In the central part of the island, regional seismicity indicates distributed deformation (Escuder-Viruete et al., 2023), but its localization or the amount of strain involved remain to be determined. In the northern Dominican Republic, where the Septentrional fault is supposedly well–mapped (Mann et al., 1998; Prentice et al., 2003), structural and geomorphological studies indicate active, distributed faulting on several fault splays off the main fault trace (Escuder-Viruete & Pérez, 2020). The next step in our understanding of active faulting and related hazard in Hispaniola therefore requires a dense and spatially–continuous velocity field across the island in order to fully capture strain partitioning and possible slip deficit on structures other than the few active fault traces currently known.

InSAR is now mature enough to build high–resolution, high–density velocity fields over large regions (e.g. Ou et al., 2022; Fang et al., 2024) with automatic processing services now available (e.g. Thollard et al., 2021). Several studies on Hispaniola have used data from various SAR constellations (ALOS–1 and 2, and Sentinel–1), focusing on individual earthquakes or their subsequent postseismic effects (Hayes et al., 2010; Calais et al., 2010; Wdowinski & Hong, 2011; Symithe et al., 2013; Saint Fleur et al., 2015; Calais et al., 2022; Raimbault et al., 2023, 2025). To date, there is however no regional-scale InSAR-derived ground velocity map available, despite the available SAR data archive.

In the following, we couple the analysis of SAR data through a Persistent Scatterer Interferometry approach to the available GNSS-derived velocity field to produce a high–resolution map of ground motion rate covering the entire island of Hispaniola. We describe in detail the processing strategy and discuss the main features of the resulting velocities, which we validate by focusing the interpretation on the major known active fault systems.

2 PSInSAR Velocities

2.1 SAR Data Processing

We consider all available SAR data acquired by the Sentinel–1 constellation from 2014 to February 2023 over the island of Hispaniola. This results in 3 ascending and 3 descending tracks for a total of 979 Single Look Complex (SLC) images with a swath width of approximately 250 km (Figure 1A, Table 1). Over the Southern Peninsula of Haiti, we restrict our analysis to the time interval ending with the 14 August 2021 M7.2 Nippes earthquake to avoid contamination of the velocity field by possible post-seismic deformation.

We process the SAR images with the ISCE2 processing chain to compute the interferograms (ISCE, JPL/Caltech - Rosen et al., 2012). We first coregister SAR Single Look Complex (SLCs) images to a single geometry using precise orbital information provided by the European Space Agency and further enhance the coregistration using the spectral diversity approach (Fattahi et al., 2016). We remove the topographic contribution using the digital elevation model from the Shuttle Radar Topography Mission (SRTM; Farr et al., 2007).

We then use the ISCE2StaMPS routines of the JPL/Caltech ISCE software to format the data for the StaMPS processing chain directory based on the output of the ISCE stack processors (Hooper, 2004; Hooper et al., 2012). These routines generate interferograms in full resolution with reference to a single image, here chosen to be in 2019 in the middle of the time series and outside of the rain season (Supplementary Figure S1).

2.2 InSAR Persistent Scatterer Processing

Within StaMPS, we perform PS detection using a normalized amplitude dispersion criterion (Ferretti et al., 2001), which identifies pixels with a stable radar backscat-

track #	direction	# of acquisitions	# of PS
4	ascending	209	836,171
106	ascending	199	2,645,694
33	ascending	190	581,928
142	descending	186	790,235
69	descending	90	1,876,957
171	descending	105	371,175

Table 1. Sentinel–1 data used in this study with the number of persistent scatters (PS) extracted per track.

ter and therefore coherent across the interferometric time series. We use an amplitude dispersion threshold of 0.45 over which pixels are considered unstable in time for each track and split the full resolution interferograms into small overlapping patches in range and azimuth. The size of each patch is chosen in order to limit the computational burden of the processing. Phase noise is estimated under the assumption that deformation and atmospheric signals are spatially correlated, while noise is spatially uncorrelated. Phase differences between neighboring PS candidates are analyzed within a Delaunay triangulation network, and long-wavelength components are reduced using spatial filtering. The variance of the resulting residual phase is then used as an estimate of pixel-scale phase noise. PS candidates are selected by removing pixels exhibiting high and random phase behavior.

PS pixels are then weeded using the default standard deviation threshold, and the Delaunay network is pruned to remove unstable or poorly connected scatterers prior to phase unwrapping. StaMPS iteratively rejects PS with insufficient neighboring connections or poor phase behavior until the residual phase statistics converge. The wrapped phase of the selected pixels is then corrected for spatially uncorrelated look angle error using the SRTM digital elevation model (Farr et al., 2007). Patches containing selected PS pixels are then merged and unwrapped in 3D using SNAPHU (Chen & Zebker, 2002).

We use default parameters of the StaMPS processing chain, except that we activate the weed elevations step to remove possible coherent PS located on water bodies. We then correct the time series of each identified PS for spatiotemporal variations of tro-

pospheric conditions using the TRAIN toolbox that makes use of the ECMWF-ERA5 global reanalysis model (Jolivet et al., 2011; Bekaert et al., 2015). We reference the PS time series to the first acquisitions to get a cumulative position time series since the first date and fit a linear least-squares model to estimate the displacement rate. We derive the associated uncertainties from the residual misfit to the linear regression. The resulting LOS velocities obtained for each track are shown in Supplementary Figure S2.

2.3 InSAR LOS Referencing from GNSS Velocities

We then splice the LOS velocities obtained for each track into a single, continuous one. To do so, we reference velocity maps to a similar position by removing the average offset from a non-moving area for ascending and descending tracks, then reference the eastern and western tracks to the central one (Figure 3A) by estimating and removing a linear ramp in azimuth and range and a constant term in each overlapping region. For validation and referencing purposes we project the horizontal GNSS velocities available to the ascending and descending LOS geometries.

The GNSS velocities used here are a subset of approximately 700 continuous and episodic GPS stations spanning the entire Caribbean plate with some sites on the North and South American plates. The data was collected both at permanently–recording stations, and at ∼300 sites surveyed episodically over 20 years in Haiti and the Dominican Republic (Figure 1B). At campaign sites, measurements are made for a duration of 3–6 continuous days for each survey. We only use sites where surveys have repeated at least three times over a total time interval of at least 5 years. We processed the data following the method outlined in Calais, Gonzalez, et al. (2023) using the GAMIT–GLOBK software package (Herring et al., 2018), with velocities referring to the International Terrestrial Reference Frame (ITRF 2014; Altamimi et al., 2016) (Figure 1B). We update this regional solution on a regular basis, the one presented here is complete to December 2024. Uncertainties and biases on vertical velocities can reach 5–10 mm/yr, especially at the campaign sites. We therefore discard them in this study.

Using the GNSS analysis results, we adjust the velocity maps to the GNSS–derived velocities projected in the ascending or descending LOS direction by estimating a ramp in azimuth and range. The comparison between PSInSAR LOS velocities and LOS–projected GNSS velocities, shown on Figure 3, shows a good agreement overall, with a correlation

coefficient of 0.8 and 0.7 for the ascending and descending tracks, respectively. Deviations are limited to 1.3 mm/yr in the ascending geometry and 1.8 mm/yr in the descending geometry, with the largest discrepancies observed in the eastern part of the island in the descending configuration (Figure 2B).

The resulting PSInSAR maps for the ascending and descending tracks (Figure 2) show an irregular spatial sampling, different between the two maps, as expected given the PS approach used here. PSs indeed concentrate within urbanized regions or over rocky terranes, but nevertheless cover the island almost completely, with missing parts in the southern and southeastern regions of the island due to a lack of SAR acquisitions there. Over regions with rugged topography and dense vegetation, such the Central Cordillera in the Dominican Republic, the number of high–coherence pixels is lower, but restricting the analysis to these few pixels still recovers a high–precision ground displacement signal.

The ascending and descending velocities (Figure 2) both show a roughly north-south velocity gradient across the island. The opposite look directions result in a gradient of opposite signs for the ascending and descending geometries, indicative of dominantly horizontal, left-lateral motion, consistent with the known large–scale kinematics. This broad island–wide signal includes two area of steeper gradient coinciding with the Enriquillo and the Septentrional fault zones to the south and north, respectively, which are discussed in detail below.

2.4 ENU Decomposition of LOS Velocities

We decompose the ascending and descending InSAR LOS velocities (V_{asc}, V_{desc}) into eastward and combined north-up (V_E, V_{UN}) components following the approach described in Ou et al. (2022), among others. The observed LOS velocities write as

$$\begin{bmatrix} V_{asc} \\ V_{desc} \end{bmatrix} = \begin{bmatrix} -\cos(\phi_{asc})\sin(\theta_{asc})\sqrt{1-\sin^2(\theta_{asc})\cos^2(\phi_{asc})} \\ -\cos(\phi_{desc})\sin(\theta_{desc})\sqrt{1-\sin^2(\theta_{desc})\cos^2(\phi_{desc})} \end{bmatrix} \begin{bmatrix} V_E \\ V_{UN} \end{bmatrix} \quad (1)$$

where ϕ and θ are the track heading and incidence angles, respectively. We use a weighted least-squares approach to solve for V_E and V_{UN} directly from the LOS observations. This approach avoids using interpolated GNSS north velocities (V_N) to determine V_E, hence preserving the spatial resolution of the InSAR data and minimizing interpolation biases.

Here V_{UN}, represents the projection of the northward (V_N) and vertical (V_U) motions onto the north–up plane. Decomposing V_{UN} as in Ou et al. (2022) requires an additional constraint on the velocity field, which we obtain from GNSS observations. Given the higher sensitivity of InSAR to V_U and the superior quality and spatial coverage of GNSS measurements for V_N, we also interpolate GNSS-derived V_N to estimate V_U (Supplementary Figure S4). The northward component of the GNSS velocities is interpolated using a kriging approach implemented with the Pykrige Python module (Murphy et al., 2021). We fit a three-dimensional polynomial surface to the GNSS V_N observations and interpolate the short-wavelength residuals using a spherical variogram model assuming spatially correlated residuals. We then re-apply the polynomial trend to obtain the final interpolated V_N velocities (Supplementary Figure S3). Uncertainties are estimated from the kriging variance and propagated as the square root of the predicted variance at each interpolation point.

The resulting V_E and V_{UN} velocity decomposition (Figure 4) is consistent with a regional deformation primarily dominated by horizontal motion in the east–west direction. The V_E velocity component (Figure 4 A) shows 2 cm/yr of integrated left-lateral shear from north to south across the island, as expected from previous GNSS observation and kinematic block models (e.g., Symithe et al., 2015).

The combined V_{UN} component (Figure 4 B) contains significant short-wavelength signal and possibly some subtle internal deformation within Hispaniola. Since the north component derived from InSAR data in constrained by the interpolation of the GNSS velocities, most of this short-wavelength signal likely results from vertical motion. Keeping this limitation in mind, the V_U component captures localized uplift along the northernmost segment of Hispaniola, spatially associated with the previously identified sharp horizontal velocity gradients, as well as broader uplift in the southernmost part of the island, particularly in the Léogâne region affected by the 2010 earthquake and also just west of the Muertos Through. At larger scale, V_U also reveals a general pattern of subsidence of approximately 2 mm/yr extending from Port-au-Prince toward Lake Azuei.

3 Discussion

In the following, we discuss some key features derived from the velocity maps of Figure 4, focusing on the three major fault systems identified so far in Hispaniola: En-

riquillo, Septentrional, and Jérémie–Malpasse–Bahoruco. In some instances, we shall project the V_E, V_N, V_U velocity decomposition described onto fault–parallel, fault–normal, and vertical directions. To do so, we rotate the ENU velocity components into fault-based reference frame using:

$$\begin{aligned} V_{\parallel} &= V_E \sin(\theta_{\text{fault}}) + V_N \cos(\theta_{\text{fault}}) \\ V_{\perp} &= V_E \cos(\theta_{\text{fault}}) - V_N \sin(\theta_{\text{fault}}) \\ V_v &= V_U \end{aligned} \tag{2}$$

where v_v, $V_{\parallel}$, and $V_{\perp}$ are the vertical, fault–parallel, and fault–normal velocities, respectively, and θ_{fault} is the fault strike angle. We use $\theta_{\text{fault}} = 265°$ for the Enriquillo fault and $\theta_{\text{fault}} = 280°$ for the Septentrional fault.

3.1 Enriquillo Fault

Panel A on Figure 5 shows a velocity profile perpendicular to the central segment of the Enriquillo fault in the Southern Peninsula of Haiti. The fault–parallel velocity gradient is symmetrical with respect to the surface trace of the fault, with a far–field left–lateral offset of ∼6 mm/yr and a shape typical of a locked fault building-up elastic strain. Across-fault profiles further indicate that fault-normal and vertical displacement rates are below 1 mm/yr, indicating a dominantly strike-slip Enriquillo fault (Figure S5). We therefore use this data to search for the best–fit parameters of a model where the fault is represented by a vertical dislocation buried in a homogeneous elastic medium at a depth D below which it slips at a rate S (Savage & Burford, 1973). This model predicts that the horizontal surface velocity parallel to the fault, $v_{\parallel}(x)$, writes as

$$v_{\parallel}(x) = -\frac{S}{\pi} \arctan\left(\frac{x - x_0}{D}\right) + \Omega\,(x - x_0) + V_0. \tag{3}$$

where x is the distance perpendicular to the fault, x_0 the horizontal shift of the fault relative to the profile reference, Ω a linear tilt term accounting for long-wavelength velocity gradients, and V_0 a constant velocity offset.

We first estimate an optimal solution using a bounded non-linear least-squares inversion, then use this solution to initialize a Bayesian sampling of the posterior distribution with the affine-invariant ensemble Markov chain Monte Carlo sampler implemented in `emcee` (Foreman-Mackey et al., 2013; Goodman & Weare, 2010). We impose uniform bounds on all parameters, with $v_{\parallel}$ allowed to vary between −25 and 0 mm/yr, D between 1 and 40 km, V_0 between −10 and 10 mm/yr, Ω between −1 and 1 $mm.yr^{-1}.km^{-1}$ and

x_0 between −20 and 20 km. The most likely model has a slip deficit rate of 7.7±1.2 mm/yr and a locking depth of 8 ± 2 km for this segment of the Enriquillo fault, with an estimated location (black circle on Figure 2A) that coincides with the mapped surface fault trace (Table 2, see Supplementary Figure S6 for the full posterior probability distribution of the estimated parameters).

Early elastic block-modeling studies based on limited GNSS data inferred pure strike-slip rates of 7±2 mm/yr on the Enriquillo fault (Manaker et al., 2008). Subsequent ones, using an improved spatial coverage, found that the data required an additional fault-normal shortening of up to 5 mm/yr (Calais et al., 2010; Benford et al., 2012; Symithe et al., 2015), at odds with the classic view of a quasi-vertical Enriquillo fault (Saint Fleur et al., 2020; Leroy et al., 2015). Using an updated GNSS data set, Calais, Symithe, and de Lépinay (2023) showed that deformation in the Southern Peninsula of Haiti is actually spatially partitioned between pure strike-slip on the Enriquillo fault and shortening on the offshore section of the Jérémie-Malpasse–Bahoruco fault system (Figure 1), a series of reverse faults that extends along the northern coast of the Southern Peninsula of Haiti (Corbeau et al., 2016) and on–land to the east into the Cul-de-Sac basin (Symithe & Calais, 2016; Saint Fleur et al., 2019).

Model parameters	EPGF	SF west	SF east	JMBF
Strike-slip rate (mm/yr)	7.7±1.3	9.2±3.6	8.8±2.3	5.9±0.5
Dip-slip rate (mm/yr)	–	–	–	8.7±0.8
Locking depth (km)	7.9±1.5	31.9±6.2	12.2±2.8	6.6±1.5
Dip angle (°)	90 (fixed)	90 (fixed)	90 (fixed)	28±3
Fault lon. (°)				71.48±0.05
Fault lat. (°)				18.37±0.04

Table 2. Summary of the posterior parameters estimated from the Bayesian inversion of the PSInSAR–derived profiles across the Enriquillo, Septentrional, and Jérémie–Malpasse–Bahoruco faults. Parameters are reported as the median of the posterior distribution and uncertainties are quantified by the standard deviation of the posterior samples.

Figure 4A shows the velocity gradient across the Enriquillo fault is relatively unchanged from at least 72°W to 74°W. Although the 2010 and 2021 earthquakes may have

released some of the available elastic energy stored in the crust in relation to a locked Enriquillo fault, its main trace was not directly involved in either of these events (Hayes et al., 2010; Calais et al., 2010; Raimbault et al., 2023). Assuming that the 3 June 1770, M∼7.5 earthquake was the last major event that ruptured the Enriquillo fault in southern Haiti, as proposed by Hough et al. (2023), and neglecting possible creep on some of its segments, the current slip deficit rate amounts to about 2 m of cumulated slip since then. This would correspond to an event with a magnitude reaching 7 (Wells & Coppersmith, 1994) if released as a single earthquake today, a magnitude similar to the 2010 and 2021 events of the Southern Peninsula. The Enriquillo fault therefore remains a significant source of future hazard.

3.2 Septentrional Fault

Panels B and C on Figure 5 show fault-parallel velocities along two profiles perpendicular to the western and eastern sections of the Septentrional fault. We observe a gradient in surface velocity in both cases, though with a smoother shape – or longer spatial wavelength – than across the Enriquillo fault. The western profile, in particular, does not show the arc-tangent shape typically associated with a single vertical locked fault. The far–field left–lateral offset across the profiles of Figure 5B and C is on the order of 8 mm/yr. Using the same inversion procedure as described above for the Enriquillo fault, we obtain slip deficit rates of 9 ± 4 mm/yr and 9 ± 2 mm/yr, with locking depths of 32 ± 6 km and 12 ± 3 km for the western and eastern profiles, respectively (Table 2, see Supplementary Figures S7 and S8 for the full posterior probability distribution of the estimated parameters). The estimated fault location (black circles on Figure 4A) coincides with the mapped surface trace of the fault for the eastern profile, but locates 5–10 km to the south for the western one.

Offset stream terraces studied at two locations in the central Cibao Valley (Figure 1A), inside the bounds of the profile on Figure 5C, provide late Holocene slip rate estimates of 6–12 mm/yr at this specific locale along the Septentrional fault (Prentice et al., 2003). Elastic block-modeling studies to date, which all assume a single vertical Septentrional fault throughout the Cibao Valley, as described in Mann et al. (1998), consistently find a slip deficit rate ranging from 8 to 12 mm/yr (Manaker et al., 2008; Benford et al., 2012; Symithe et al., 2015), hence consistent with the paleoseismic slip re-

lease rate. The estimates derived here from PSInSAR velocities are within the range of these previous studies.

While the 12 km locking depth estimated for the eastern profile is consistent with many other similar strike-slip faults (e.g., Vernant, 2015), the 32 km found for the western one appears unreasonably large considering classic assumptions on the depth of the brittle-ductile transition (e.g., Bürgmann & Dresen, 2008). Invoking the trade–off between locking depth and slip rate in the inversion is not satisfying in this case, as the best–fitting slip rate is comparable to previously published ones. The large value directly derives from the quasi-linear change in velocity along the profile of Figure 5B which, in the classic elastic strain accumulation model of equation 3 for a single vertical fault, imposes an unrealistically large locking depth.

This quasi-linear gradient may be explained if the Septentrional fault does not localize as a single strand but splits into several splays, with low individual slip rates that still total the integrated ∼9 mm/yr far–field value. Some of these splays may be covered by the sediments brought by the Rio Yaque del Norte, the second largest river of the island, which flows north from the Central Cordillera to the central Cibao Valley, then turns west to follow the valley parallel to the Septentrional fault. In this hypothesis, the multiple sub-parallel splays would result in distributed strain, as observed in other settings (e.g., Fialko, 2006; Dalaison et al., 2023). This would be consistent with structural and geomorphological studies showing that several fault splays developed since the Middle Pleistocene (∼1.5 Ma) in the western part of the Cibao Valley (Escuder-Viruete & Pérez, 2020). The main fault trace through the lower crust would then not need to coincide with any single one of those splays, explaining why our fault location estimate is off the classically mapped one.

The dense PS-InSAR velocities described above are therefore consistent with a purely strike-slip, vertical Septentrional fault locked to 10–15 km depth in its eastern section through the northern Dominican Republic, and suggest distributed slip into several active strands along the western section. The integrated slip deficit rate is however similar over the entire length of the Septentrional fault system. Given the long time interval since the last large earthquake in the northern Dominican Republic – 1652 A.D. at least – the Septentrional fault system has likely accumulated elastic strain sufficient to generate a major earthquake, as many authors have pointed out (e.g., Mann et al., 1998;

Prentice et al., 2003; Manaker et al., 2008), though hazard may be more broadly distributed than previously though in the western part of the Cibao Valley.

3.3 Jérémie–Malpasse–Bahoruco Fault

The geometry and sense of motion of the continuation of the Enriquillo fault east of the Southern Peninsula into the Cul-de-Sac and Enriquillo basins is the subject of a debate. For some, the fault continues as a vertical strike-slip fault along the southern edge of the Cul-de-Sac basin in Haiti and eastward into the Enriquillo basin in the Dominican Republic (e.g. Mann et al., 1995; Wang et al., 2018). In that interpretation, the folding that affects Plio-Quaternary sediments in these basins are en échelon drag folds associated with strike-slip faulting. For others, the Enriquillo fault throughout the Southern Peninsula abuts against a north-verging reverse fault system that marks the southern edge of the Cul-de-Sac and Enriquillo basins (e.g. Bourgueil et al., 1988; Saint Fleur et al., 2020; Escuder-Viruete et al., 2025). In that interpretation, Plio-Quaternary sediments of the two basins are folded as a result of active north–verging thrusting of the La Selle (Haiti) and Bahoruco (Dominican Republic) ranges along the onshore section of the Jérémie–Malpasse fault in Haiti, continuous eastward with the Bahoruco fault in the Dominican Republic (Figure 1). Symithe and Calais (2016) showed that this later hypothesis was consistent with GNSS measurements in Haiti, though their data set was very sparse.

Figure 6 shows 3–component velocity profiles perpendicular to the Bahoruco/La Selle range – Enriquillo/Cul-de-Sac basin system derived from our 3D PSInSAR data. The encompassing area overlays that used in Symithe and Calais (2016), though with a much denser data set. Importantly, the PSInSAR data provides vertical velocities, in addition to the fault–normal and fault–perpendicular velocity components. The profiles indicate a combination of (1) uplift of the La Selle/Bahoruco range with respect to the Enriquillo/Cul-de-Sac basin at ∼3 mm/yr, (2) shortening at ∼6 mm/yr, and (3) left–lateral strike–slip at ∼5 mm/yr. The velocity gradients localize at the contact between the La Selle/Bahoruco range and the Enriquillo/Cul-de-Sac basin. The fault–parallel and fault–perpendicular ones are remarkably similar in shape and amplitude to the ones presented by Symithe and Calais (2016). As an aside, we note here that the PS-InSAR velocities do not show evidence for strain localization along the northern edge of the Enriquillo/Cul-

de-Sac basin, indicating that the front of the Matheux–Neiba range (Figure 6D) is likely inactive.

We model these profiles approximating the fault system as a single dislocation buried in an elastic half–space. The dislocation is parameterized by along–strike and down–dip slip, a locking depth, a dip angle, as well as a horizontal shift relative to the profile reference point. This allows us to estimate the best-fit fault dip and location as free parameters. The fault-parallel velocity, $v_{\parallel}(x)$, for a vertical dislocation buried at a depth D below which it slips at a rate S writes as

$$v_{\parallel}(x) = -\frac{V_{\mathrm{ss}}}{\pi} \arctan\left(\frac{x - c_x}{D}\right) + b_{\parallel}, \tag{4}$$

where V_{ss} is the strike-slip rate, c_x the across-profile position of the fault, and $b_{\parallel}$ a constant velocity offset Savage and Burford (1973). The fault–normal, $v_{\perp}(x)$, and vertical, $v_z(x)$, velocities are modeled following Segall (2010) and write as

$$v_{\perp}(x) = \frac{V_{ds}}{\pi}\left[\cos\delta \arctan\gamma + \frac{\sin\delta - \gamma\cos\delta}{1+\gamma^2}\right] + b_{\perp} \tag{5}$$

$$v_z(x) = -\frac{V_{ds}}{\pi}\left[\sin\delta \arctan\gamma + \frac{\cos\delta + \gamma\sin\delta}{1+\gamma^2}\right] + b_z, \tag{6}$$

with

$$\gamma = \frac{x - c_x}{D}. \tag{7}$$

Here V_{ds} is the dip-slip rate, δ the fault dip, and $b_{\perp}$ and b_z are constant offsets for the fault-normal and vertical velocity components, respectively.

We estimate the model parameters using the same Bayesian framework and tools as described above. We impose uniform bounds on all parameters, with V_{ss} and V_{ds} allowed to vary between -15 and 15 mm/yr, D between 1 and 15 km, δ between 90° and 180°, and c_x between -35 and 35 km. Gaussian priors are additionally imposed on the locking depth and dip, with $D = 7 \pm 3$ km and $\delta = 150 \pm 5°$. The best-fit model parameters (Table 2, see Supplementary Figures S9 for the full posterior probability distribution of the estimated parameters) are remarkably similar to the ones estimated by Symithe and Calais (2016, Table 1), though with a shallower fault dip angle, still consistent within uncertainty bounds. The surface projection of the buried dislocation (Figure 6E) corresponds to the active folds identified in the Cul-de-Sac basin by Saint Fleur et al. (2020) and in the Enriquillo basin by Escuder-Viruete et al. (2025). These are likely fault-propagation folds that develop on top of décollements rooted in the south-dipping reverse fault.

Horizontal gradients in PSInSAR velocities are therefore consistent with a combination of reverse (∼9 mm/yr) and strike-slip (∼6 mm/yr) faulting on a south–dipping fault along the southern edge of the Cul-de-Sac/Enriquillo basin. It is of course possible than more than one fault is involved in this process as the geodetic data would smooth out strain build up on nearby faults. This fault materializes the onshore section of the Jérémie–Malpasse fault in Haiti and its eastward continuation into the Dominican Republic as the Bahoruco fault, consistent with the north–dipping structure identified under the La Selle/Bahoruco range from earthquake hypocenters, focal mechanisms, and seismic tomography (Possee et al., 2019; Rodriguez et al., 2018). When projected to the surface, the total slip rate on the fault corresponds to 7.7±0.7 mm/yr of horizontal shortening, a value that is similar to independent estimates of microplate motions from regional–scale kinematic block models (Calais, Symithe, & de Lépinay, 2023).

Among the historical events that struck southern Hispaniola, the 18 October 1751 and 21 November 1751 ones, with intensity magnitudes of 7.5 and 6.6, are of particular interest here. Their epicenters have indeed been located by Bakun et al. (2012) on the eastern end of the Enriquillo basin for the former, at the western end of the Cul-de-Sac basin for the latter (Figure 1A). Given its proposed epicenter, the 21 November 1751 may have struck the Enriquillo strike-slip fault, or equally likely the Jérémie–Malpasse oblique–reverse fault near Port-au-Prince. The 18 October 1751 event, particularly destructive, has been associated to the Muertos thrust offshore (McCann, 2006; Ali et al., 2008). However, Bakun et al. (2012), using a detailed reanalysis of historical intensities with a grid search technique that accounts for ground motion attenuation, *"favor an onshore location near the east end of the Enriquillo fault system"*. This location is compatible with a rupture of the Jérémie–Malpasse fault system in that area, though other candidates are possible (Escuder-Viruete et al., 2025).

The slip deficit rates estimated here amount to recurrence rates of ∼285 years and ∼900 years for Mw7.0 and Mw7.5 earthquakes, respectively (Wells & Coppersmith, 1994). Assuming elastic strain build up and release on a single fault, this implies that the Jérémie–Malpasse–Bahoruco oblique–reverse fault currently has the potential for a Mw7.0 earthquake. In addition, Symithe and Calais (2016) showed that such a rupture on a north-dipping oblique–slip fault would produce significantly more ground shaking than an equivalent one on a vertical, pure strike–slip one. The hazard level posed by the onshore section of the Jérémie–Malpasse–Bahoruco fault through the Cul-de-Sac/Enriquillo basin

should therefore be considered significant. This fault system should be explicitly accounted for in the source models that underlie earthquake hazard maps for Haiti and the Dominican Republic (e.g. Frankel et al., 2011; Johnson et al., 2024).

4 Conclusions

By combining line-of-sight velocities from a Persistent Scatterer Interferometry (PSInSAR) analysis of Sentinel-1 data with the most recent GNSS velocities from continuous and episodic observations in Hispaniola, we determine a spatially-continuous 3D velocity field for the island that documents deformation gradients across large fault systems. We focus its interpretation on the major known active fault systems in order to validate the resulting velocities against independent information, and provide additional insights on the characteristics of these faults and the implication on earthquake hazard.

We find that the Enriquillo fault through the Southern Peninsula of Haiti fits a single locked–fault model, with pure strike-slip at a rate of 8±1 mm/yr, consistent within uncertainties with several regional kinematic block models based on GPS velocities only. The velocity gradient across the Septentrional fault in the northern Dominican Republic encompasses an area broader than typically assumed, in particular in its western section where the fault trace is not clearly identified in the morphology. This likely indicates that the fault actually consists of several active splays, as proposed by Escuder-Viruete and Pérez (2020). The best–fitting single fault model finds pure strike-slip at a rate of 9±3 mm/yr, but the large uncertainties, as well as the large locking depth inferred for its western section, indicate that more complex models are required. Regional earthquake hazard models should consider, in the northern Dominican Republic, a broader earthquake source distribution than a single Septentrional fault.

In southeastern Haiti and the southwestern Dominican Republic, the PSInSAR–derived velocities are consistent with oblique reverse slip on a single south–dipping fault that allows for the thrusting of the La Selle/Bahoruco ranges over the Cul-de-Sac/Enriquillo basin. That fault coincides with the onshore section of the Jérémie–Malpasse–Bahoruco fault system proposed in previous studies on the basis of geological, seismological, and sparse geodetic data. This fault system, overlooked in hazard studies to date, should explicitly be accounted for in future regional earthquake hazard models.

More detailed analyses of this PSInSAR–derived velocity field will likely provide additional information on strain distribution within the island, aseismic slip on some faults or fault segments, slip on potential slow faults yet to be identified, and vertical motions related to tectonic and anthropogenic processes. The increasing availability of long InSAR time series and upcoming missions such as NISAR will further enhance our ability to address these issues.

5 Open Research Statement

Processed PSInSAR data, along with the derived fault data that support the findings and are necessary to reproduce the results presented in this study, have been deposited in a public repository at Zenodo (Raimbault et al., 2026). We use Copernicus data from the Sentinel-1AB satellites, freely provided by the European Space Agency (ESA, `https://browser.dataspace.copernicus.eu)`, which can be accessed after user registration and a review of the documentation available on the website. Shuttle Radar Topography Mission (SRTM) 1 Arc-Second Global data was retrieved from USGS Archive (Farr et al., 2007). The ISCE2 open-source software used to process the SAR images is freely available to download from `https://github.com/isce-framework/isce2/releases/tag/v2.6.3` (Rosen et al., 2012). The StaMPS software used to do the PS analysis is freely available to download from https://github.com/dbekaert/StaMPS/releases/tag/v4.1-beta (Hooper, 2004). The TRAIN package for the tropospheric correction of PS is available from: `https://github.com/dbekaert/TRAIN/releases/tag/v3.beta` (Bekaert et al., 2015). We use the Classic Slip Inversion (CSI) package available at `https://github.com/jolivetr/csi/releases/tag/1.0.0` for the generation of profiles across faults, slip inversions, plotting, and handling of the geodetic data. The authors highly recommend obtaining the latest versions of the codes from the GitHub repository. This ensures access to the most up-to-date version, as any other versions available elsewhere are likely to be outdated.

Acknowledgments

We thank ESA for acquiring and distributing continuous and freely available SAR imagery datasets. RJ acknowledges funding from the Institut Universitaire de France. SS acknowledges funding from the "Fonds d'Appui à la Recherche" of the Rectorat of the State University of Haiti, and the USAID's Bureau of Humanitarian Assistance via the

Grant and Cooperative Agreement between U.S. Geological Survey (G20AC00100) and the Faculté Des Sciences of the State University of Haiti. This project has received funding from the European Research Council (ERC) under the European Union's Horizon 2020 research and innovation program (Grant 758210 for project Geo4D and Grant 1101125232 for project iQuake), and from the French National Research Agency (Projects ANR-21CE03-0010 "OSMOSE", ANR-22-CE01-0019 "CAST", and ANR-19-P3IA-0003 "MIAI@Grenoble Alpes").

References

Ali, S. T., Freed, A. M., Calais, E., Manaker, D. M., & McCann, W. R. (2008). Coulomb stress evolution in Northeastern Caribbean over the past 250 years due to coseismic, postseismic and interseismic deformation. *Geophysical Journal International*, *174*(3), 904–918. doi: 10.1111/j.1365-246X.2008.03634.x

Altamimi, Z., Rebischung, P., Métivier, L., & Collilieux, X. (2016). ITRF2014: A new release of the International Terrestrial Reference Frame modeling nonlinear station motions. *Journal of Geophysical Research-Solid Earth*, *121*(8), 6109–6131. doi: 10.1002/2016JB013098

Bakun, W. H., Flores, C. H., & ten Brink, U. S. (2012). Significant Earthquakes on the Enriquillo Fault System, Hispaniola, 1500–2010: Implications for Seismic Hazard. *Bulletin of the Seismological Society of America*, *102*(1), 18–30. doi: 10.1785/0120110077

Bekaert, D. P. S., Walters, R. J., Wright, T. J., Hooper, A. J., & Parker, D. J. (2015). Statistical comparison of InSAR tropospheric correction techniques. *Remote Sensing of Environment*, *170*(C), 40–47. doi: 10.1016/j.rse.2015.08.035

Benford, B., DeMets, C., & Calais, E. (2012). GPS estimates of microplate motions, northern Caribbean: evidence for a Hispaniola microplate and implications for earthquake hazard. *Geophysical Journal International*, *191*(2), 481-490. doi: 10.1111/j.1365-246X.2012.05662.x

Bourgueil, B., Andreieff, P., Lasnier, J., Gonnard, R., Le Metour, J., & Rancon, J.-P. (1988). *Synthèse Géologique de la République d'Haiti* (BRGM-Beicip No. Volume 1 Géologie). Haiti, Port-au-Prince: Bureau des Mines et de l'Energie.

Bürgmann, R., & Dresen, G. (2008). Rheology of the Lower Crust and Upper Man-

514 tle: Evidence from Rock Mechanics, Geodesy, and Field Observations. *Annual*
515 *Review of Earth and Planetary Sciences*, *36*(1), 531–567. doi: 10.1146/annurev
516 .earth.36.031207.124326

517 Burke, K. (1988). Tectonic evolution of the Caribbean. *Annual review of Earth and*
518 *Planetary Sciences*, *16*, 201–230.

519 Calais, E., Béthoux, N., & De Lépinay, B. M. (1992). From transcurrent fault-
520 ing to frontal subduction: A seismotectonic study of the Northern Caribbean
521 Plate Boundary from Cuba to Puerto Rico. *Tectonics*, *11*(1), 114–123. doi:
522 10.1029/91TC02364

523 Calais, E., Freed, A., Mattioli, G., Amelung, F., Sigurjón, J., Jansma, P., ... Mom-
524 plaisir, R. (2010). Transpressional rupture of an unmapped fault during the
525 2010 Haiti earthquake. *Nature Geoscience*, *3*(11), 1–6. doi: 10.1038/ngeo992

526 Calais, E., Gonzalez, O., Arango-Arias, E., Moreno, B., Palau, R., Cutie, M., ...
527 Symithe, S. (2023). Current deformation along the northern Caribbean plate
528 boundary from GNSS measurements in Cuba. *Tectonophysics*, *868*, 230068.
529 doi: 10.1016/j.tecto.2023.230068

530 Calais, E., Symithe, S. J., & de Lépinay, B. M. (2023). Strain partitioning within
531 the caribbean–north america transform plate boundary in southern haiti,
532 tectonic and hazard implications. *Bulletin of the Seismological Society of*
533 *America*, *113*(1), 131–142. doi: 10.1785/0120220121

534 Calais, E., Symithe, S. J., Monfret, T., Delouis, B., Lomax, A., Courboulex, F., ...
535 Meng, L. (2022). Citizen seismology helps decipher the 2021 Haiti earthquake.
536 *Science*, *376*(6590), 283-287. doi: 10.1126/science.abn1045

537 Chen, C., & Zebker, H. (2002). Phase unwrapping for large SAR interfero-
538 grams: statistical segmentation and generalized network models. *IEEE*
539 *Transactions on Geoscience and Remote Sensing*, *40*(8), 1709-1719. doi:
540 10.1109/TGRS.2002.802453

541 Corbeau, J., Rolandone, F., Leroy, S., Meyer, B., Mercier de Lépinay, B., Ellouz-
542 Zimmermann, N., & Momplaisir, R. (2016). How transpressive is the
543 northern Caribbean plate boundary? *Tectonics*, *35*(4), 1032-1046. doi:
544 10.1002/2015TC003996

545 Dalaison, M., Jolivet, R., & Pourhiet, L. L. (2023). A snapshot of the long-term evo-
546 lution of a distributed tectonic plate boundary. *Science Advances*, *9*(16). doi:

10.1126/sciadv.add7235

DeMets, C., Jansma, P. E., Mattioli, G. S., Dixon, T. H., Farina, F., Bilham, R., ... Mann, P. (2000). GPS geodetic constraints on Caribbean-North America Plate Motion. *Geophysical Research Letters*, *27*(3), 437-440. doi: 10.1029/1999GL005436

Douilly, R., Haase, J. S., Ellsworth, W. L., Bouin, M.-P., Calais, E., Symithe, S. J., ... Hough, S. E. (2013). Crustal Structure and Fault Geometry of the 2010 Haiti Earthquake from Temporary Seismometer Deployments. *Bulletin of the Seismological Society of America*, *103*(4), 2305–2325. doi: 10.1785/0120120303

Douilly, R., Paul, S., Monfret, T., Deschamps, A., Ambrois, D., Symithe, S. J., ... Chèze, J. (2023). Rupture Segmentation of the 14 August 2021 Mw 7.2 Nippes, Haiti, Earthquake Using Aftershock Relocation from a Local Seismic Deployment. *Bulletin of the Seismological Society of America*, *113*(1), 58–72. doi: 10.1785/0120220128

Escuder-Viruete, J., & Pérez, Y. (2020). Neotectonic structures and stress fields associated with oblique collision and forearc sliver formation in northern Hispaniola: Implications for the seismic hazard assessment. *Tectonophysics*, *784*, 228452. doi: 10.1016/j.tecto.2020.228452

Escuder-Viruete, J., Fernández, F. J., Valera, F. P., & Medialdea, A. (2023). Present-Day Caribbean-North American Oblique Convergence Through the Ocoa-Bonao-La Guacara Fault Zone, Southern Central Hispaniola: A Transition Zone Between Oceanic Subduction and Arc-Oceanic Plateau Collision. *Tectonics*, *42*(4). doi: 10.1029/2022TC007618

Escuder-Viruete, J., Fernández, F. J., Valera, F. P., Medialdea, A., & Castillo-Carrión, M. (2025). Present–Day Shortening Accommodated by Folding, Thrusting and Strike–Slip Faulting in the Enriquillo Basin of Southern Central Hispaniola: Implications for the Regional Seismic Hazard. *Tectonics*, *44*(1). doi: 10.1029/2024TC008376

Fang, J., Houseman, G. A., Wright, T. J., Evans, L. A., Craig, T. J., Elliott, J. R., & Hooper, A. (2024). The Dynamics of the India–Eurasia Collision: Faulted Viscous Continuum Models Constrained by High–Resolution Sentinel–1 InSAR and GNSS Velocities. *Journal of Geophysical Research: Solid Earth*, *129*(6).

doi: 10.1029/2023JB028571

Farr, T. G., Rosen, P. A., Caro, E., Crippen, R., Duren, R., Hensley, S., ... Alsdorf, D. (2007). The Shuttle Radar Topography Mission. *Reviews of Geophysics*, *45*(2). doi: 10.1029/2005RG000183

Fattahi, H., Agram, P., & Simons, M. (2016). A Network-Based Enhanced Spectral Diversity Approach for TOPS Time-Series Analysis. *IEEE Transactions on Geoscience and Remote Sensing*, 1–10. doi: 10.1109/TGRS.2016.2614925

Ferretti, A., Prati, C., & Rocca, F. (2001). Permanent scatterers in SAR interferometry. *IEEE Transactions on Geoscience and Remote Sensing*, *39*(1), 8–20. doi: 10.1109/36.898661

Fialko, Y. (2006). Interseismic strain accumulation and the earthquake potential on the southern San Andreas fault system. *Nature*, *441*(7096), 968–971. doi: 10.1038/nature04797

Foreman-Mackey, D., Hogg, D. W., Lang, D., & Goodman, J. (2013). emcee: The MCMC Hammer. *Publications of the Astronomical Society of the Pacific*, *125*(925), 306. doi: 10.1086/670067

Frankel, A., Harmsen, S., Mueller, C., Calais, E., & Haase, J. (2011). Seismic Hazard Maps for Haiti. *Earthquake Spectra*, *27*(1S1), 23–41. doi: 10.1193/1.3631016

Goodman, J., & Weare, J. (2010). Ensemble samplers with affine invariance. *Commun. Appl. Math. Comput. Sc.*, *5*(1), 65–80. doi: 10.2140/camcos.2010.5.65

Hayes, G. P., Briggs, R. W., Sladen, A., Fielding, E. J., Prentice, C., Hudnut, K., ... Simons, M. (2010). Complex rupture during the 12 January 2010 Haiti earthquake. *Nature Geoscience*, *3*(11), 800–805. doi: 10.1038/ngeo977

Herring, T., King, R., Floyd, M., & McClusky, S. (2018). Introduction to GAMIT/GLOBK. *Massachusetts Institute of Technology, Cambridge, Massachusetts*.

Hooper, A. (2004). A new method for measuring deformation on volcanoes and other natural terrains using InSAR persistent scatterers. *Geophysical Research Letters*, *31*(23). doi: 10.1029/2004GL021737

Hooper, A., Bekaert, D., Spaans, K., & Arıkan, M. (2012). Recent advances in SAR interferometry time series analysis for measuring crustal deformation. *Tectonophysics*, *514-517*(C), 1–13. doi: 10.1016/j.tecto.2011.10.013

Hough, S. E., Martin, S. S., Symithe, S. J., & Briggs, R. (2023). Rupture Scenarios for the 3 June 1770 Haiti Earthquake. *Bulletin of the Seismological Society of America*, *113*(1), 157–185. doi: 10.1785/0120220108

Johnson, K., Chartier, T., Pagani, M., Perez, Y., Guzman, V., De Medina, M. B. R., ... Yepes-Estrada, C. (2024). Probabilistic seismic hazard analysis for the Dominican Republic. *Earthquake Spectra*, *40*(4), 2504–2544. doi: 10.1177/87552930241263618

Jolivet, R., Grandin, R., Lasserre, C., Doin, M. P., & Peltzer, G. (2011). Systematic InSAR tropospheric phase delay corrections from global meteorological reanalysis data. *Geophysical Research Letters*, *38*(17). doi: 10.1029/2011GL048757

Leroy, S., Ellouz-Zimmermann, N., Corbeau, J., Rolandone, F., de Lépinay, B. M., Meyer, B., ... Muñoz, S. (2015). Segmentation and kinematics of the north america-caribbean plate boundary offshore hispaniola. *Terra Nova*, *27*(6), 467-478. doi: 10.1111/ter.12181

Manaker, D. M., Calais, E., Freed, A. M., Ali, S. T., Przybylski, P., Mattioli, G., ... De Chabalier, J. B. (2008). Interseismic Plate coupling and strain partitioning in the Northeastern Caribbean. *Geophysical Journal International*, *174*(3), 889-903. doi: 10.1111/j.1365-246X.2008.03819.x

Mann, P., Calais, E., Ruegg, J.-C., DeMets, C., Jansma, P. E., & Mattioli, G. S. (2002). Oblique collision in the northeastern Caribbean from GPS measurements and geological observations. *Tectonics*, *21*(6). doi: 10.1029/2001TC001304

Mann, P., Prentice, C. S., Burr, G., Peña, L. R., & Taylor, F. W. (1998). Tectonic geomorphology and paleoseismology of the Septentrional fault system, Dominican Republic. In *Active Strike-Slip and Collisional Tectonics of the Northern Caribbean Plate Boundary Zone* (pp. 63–123). Geological Society of America. doi: 10.1130/0-8137-2326-4.63

Mann, P., Taylor, F., Edwards, R., & Ku, T.-L. (1995). Actively evolving microplate formation by oblique collision and sideways motion along strike-slip faults: An example from the northeastern caribbean plate margin. *Tectonophysics*, *246*(1), 1-69. doi: 10.1016/0040-1951(94)00268-E

Martin, S. S., & Hough, S. E. (2022). The 8 April 1860 Jour de Pâques Earthquake Sequence in Southern Haiti. *Bulletin of the Seismological Society of America*,

112(5), 2468–2486. doi: 10.1785/0120220016

McCaffrey, R. (2013). Crustal Block Rotations and Plate Coupling. In S. Stein & J. T. Freymueller (Eds.), *Geodynamics Series* (pp. 101–122). Washington, D. C.: American Geophysical Union. doi: 10.1029/GD030p0101

McCann, W. R. (2006). Estimating the threat of tsunamigenic earthquakes and earthquake induced-landslide tsunami in the caribbean. In *Caribbean tsunami hazard* (pp. 43–65). World Scientific.

Meade, B. J., & Loveless, J. P. (2009). Block Modeling with Connected Fault-Network Geometries and a Linear Elastic Coupling Estimator in Spherical Coordinates. *Bulletin of the Seismological Society of America*, *99*(6), 3124–3139. doi: 10.1785/0120090088

Murphy, B., Müller, S., & Yurchak, R. (2021). *Geostat-framework/pykrige: v1.6.1.* Zenodo. doi: 10.5281/zenodo.5380342

Ou, Q., Daout, S., Weiss, J. R., Shen, L., Lazecký, M., Wright, T. J., & Parsons, B. E. (2022). Large-scale interseismic strain mapping of the ne tibetan plateau from sentinel-1 interferometry. *Journal of Geophysical Research: Solid Earth*, *127*(6). doi: 10.1029/2022JB024176

Patriat, M., Pichot, T., Westbrook, G., Umber, M., Deville, E., Bénard, F., ... the ANTIPLAC Cruise Party (2011). Evidence for Quaternary convergence across the North America–South America plate boundary zone, east of the Lesser Antilles. *Geology*, *39*(10), 979-982. doi: 10.1130/G32474.1

Possee, D., Keir, D., Harmon, N., Rychert, C., Rolandone, F., Leroy, S., ... Prépetit, C. (2019). The Tectonics and Active Faulting of Haiti from Seismicity and Tomography. *Tectonics*, *38*(3), 1138–1155. doi: 10.1029/2018TC005364

Prentice, C. S., Mann, P., Peña, L. R., & Burr, G. (2003). Slip rate and earthquake recurrence along the central septentrional fault, north american–caribbean plate boundary, dominican republic. *Journal of Geophysical Research: Solid Earth*, *108*(B3). doi: 10.1029/2001JB000442

Raimbault, B., Jolivet, R., Calais, E., Fukushima, Y., & Symithe, S. (2025). Weak and shallow secondary frictional faults revealed by large earthquakes in haiti. *Geophysical Research Letters*, *52*(18). doi: 10.1029/2025GL114939

Raimbault, B., Jolivet, R., Calais, E., Symithe, S., & Emmanuel, C. (2026). *Dataset*

for manuscript: Current deformation in hispaniola from insar–derived surface velocities. Zenodo. doi: 10.5281/zenodo.20094478

Raimbault, B., Jolivet, R., Calais, E., Symithe, S., Fukushima, Y., & Dubernet, P. (2023). Rupture geometry and slip distribution of the mw 7.2 nippes earthquake, haiti, from space geodetic data. *Geochemistry, Geophysics, Geosystems*, *24*(4). doi: 10.1029/2022GC010752

Rodriguez, J., Havskov, J., Sørensen, M. B., & Santos, L. F. (2018). Seismotectonics of south-west Dominican Republic using recent data. *Journal of Seismology*, *22*(4), 883–896. doi: 10.1007/s10950-018-9738-9

Rosen, P. A., Gurrola, E., Sacco, G. F., & Zebker, H. (2012). The InSAR scientific computing environment. In *Eusar 2012; 9th european conference on synthetic aperture radar* (p. 730-733).

Saint Fleur, N., Feuillet, N., & Klinger, Y. (2019). Active tectonics along the Cul-de-Sac – Enriquillo plain and seismic hazard for Port-au-Prince, Haiti. *Tectonophysics*, *771*, 228235. doi: 10.1016/j.tecto.2019.228235

Saint Fleur, N., Klinger, Y., & Feuillet, N. (2020). Detailed map, displacement, paleoseismology, and segmentation of the Enriquillo-Plantain Garden Fault in Haiti. *Tectonophysics*, *778*, 228368. doi: 10.1016/j.tecto.2020.228368

Saint Fleur, N., Feuillet, N., Grandin, R., Jacques, E., Weil-Accardo, J., & Klinger, Y. (2015). Seismotectonics of southern haiti: A new faulting model for the 12 january 2010 m7.0 earthquake. *Geophysical Research Letters*, *42*(23), 10,273-10,281. doi: 10.1002/2015GL065505

Savage, J. C., & Burford, R. O. (1973). Geodetic determination of relative plate motion in central California. *Journal of Geophysical Research*, *78*(5), 832–845. doi: 10.1029/JB078i005p00832

Scherer, J. (1912). Great earthquakes in the Island of Haiti. *Bulletin of the Seismological Society of America*, *2*(3), 161–180. doi: 10.1785/BSSA0020030161

Segall, P. (2010). *Earthquake and volcano deformation.* Princeton University Press. doi: 10.1515/9781400833856

Symithe, S., & Calais, E. (2016). Present-day shortening in Southern Haiti from GPS measurements and implications for seismic hazard. *Tectonophysics*, *679*, 117–124. doi: 10.1016/j.tecto.2016.04.034

Symithe, S., Calais, E., Chabalier, J.-B. d., Robertson, R., & Higgins, M. (2015).

Current block motions and strain accumulation on active faults in the Caribbean. *Journal of Geophysical Research-Solid Earth*, *120*(5), 3748–3774. doi: 10.1002/2014JB011779

Symithe, S., Calais, E., Haase, J. S., Freed, A. M., & Douilly, R. (2013). Coseismic Slip Distribution of the 2010 M 7.0 Haiti Earthquake and Resulting Stress Changes on Regional Faults. *Bulletin of the Seismological Society of America*, *103*(4), 2326-2343. doi: 10.1785/0120120306

Thollard, F., Clesse, D., Doin, M.-P., Donadieu, J., Durand, P., Grandin, R., ... Specht, B. (2021). FLATSIM: The ForM@Ter LArge-Scale Multi-Temporal Sentinel-1 InterferoMetry Service. *Remote Sensing*, *13*(18). doi: 10.3390/rs13183734

Vernant, P. (2015). What can we learn from 20years of interseismic GPS measurements across strike-slip faults? *Tectonophysics*, *644-645*, 22–39. doi: 10.1016/j.tecto.2015.01.013

Wang, J., Mann, P., & Stewart, R. R. (2018). Late Holocene Structural Style and Seismicity of Highly Transpressional Faults in Southern Haiti. *Tectonics*, *37*(10), 3834–3852. doi: 10.1029/2017TC004920

Wdowinski, S., & Hong, S.-H. (2011). Postseismic deformation following the 2010 Haiti earthquake: Time-dependent surface subsidence induced by groundwater flow in response to a sudden uplift. In *Proceedings of the Fringe 2011 Workshop* (Vol. 5). Frascati, Italy.

Wells, D. L., & Coppersmith, K. J. (1994). New empirical relationships among magnitude, rupture length, rupture width, rupture area, and surface displacement. *Bulletin of the Seismological Society of America*, *84*(4), 974–1002. doi: 10.1785/BSSA0840040974

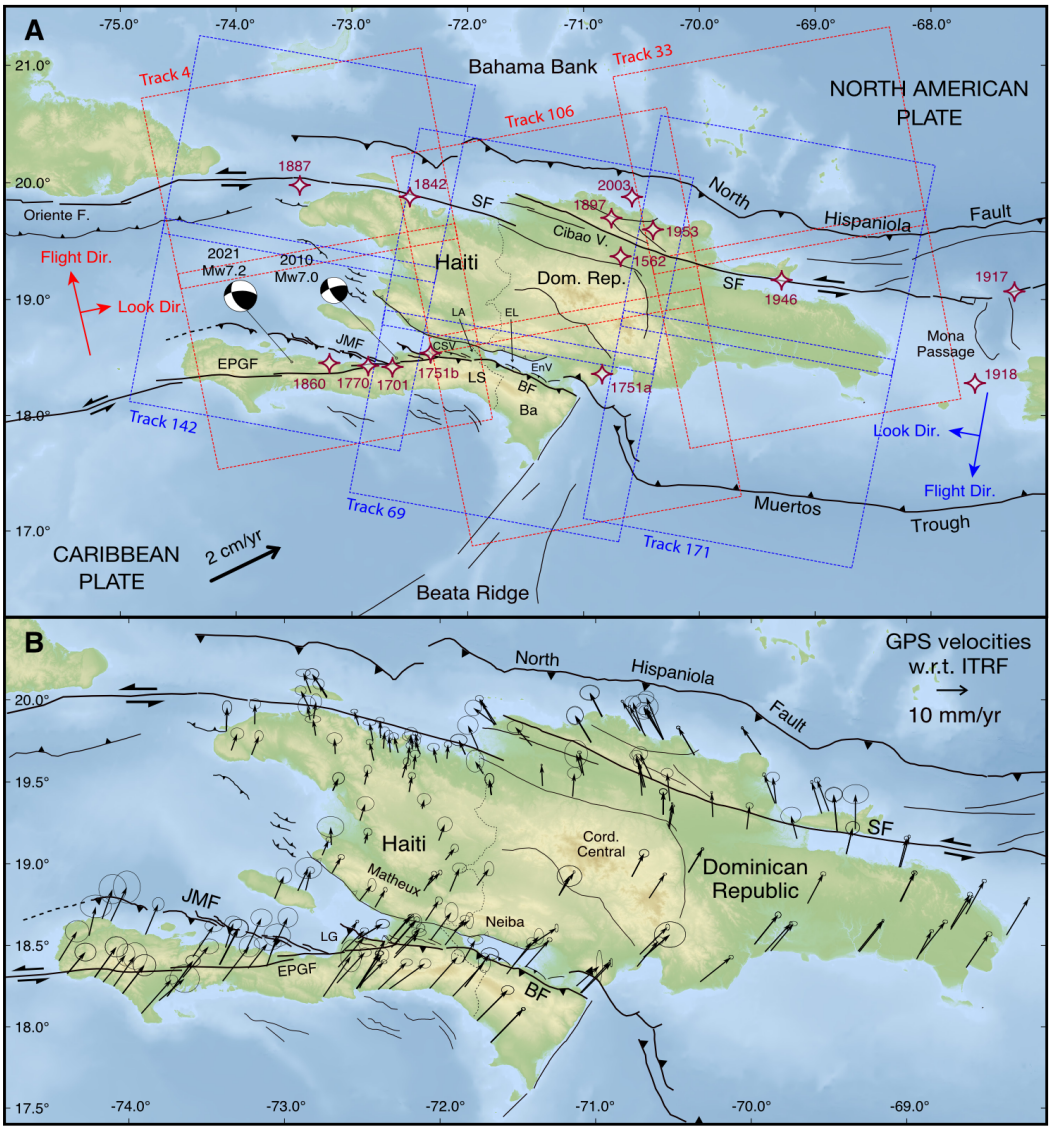

Figure 1. Seismotectonic context of Hispaniola and geodetic data sets used in this study. Black lines are active fault traces (Saint Fleur et al., 2020; Calais, Symithe, & de Lépinay, 2023; Escuder-Viruete et al., 2023, 2025). **A:** Red rectangles show the footprint of the Sentinel-1 A/B frames for tracks 4, 106, and 33 in the ascending geometry (geometry of acquisition is shown by the red arrows). Blue rectangles show the footprint of the Sentinel-1 A/B frames for tracks 142, 69, and 171 in the descending geometry (geometry of acquisition is shown by the blue arrows). White stars indicate major historical earthquakes (Scherer, 1912; Bakun et al., 2012; Martin & Hough, 2022; Hough et al., 2023). Focal mechanisms for the Léogâne (Mw7.0, 12 January 2010) and Nippes (Mw 7.2, 14 August 2021) earthquakes are from USGS. **B:** GNSS–derived velocities (black arrows) shown with respect to the International Terrestrial Reference Frame (ITRF2014; Altamimi et al., 2016). Error ellipses are 95% confidence. EPGF: Enriquillo Plaintain Garden Fault; JMF: Jérémie-Malpasse Fault; BF: Baoruco Fault; SF: Septentrional Fault; CSV: Cul-de-Sac Valley; EnV: Enriquillo Valley; LG: Léogâne; LA: Lake Azuei; EL: Enriquillo Lake.

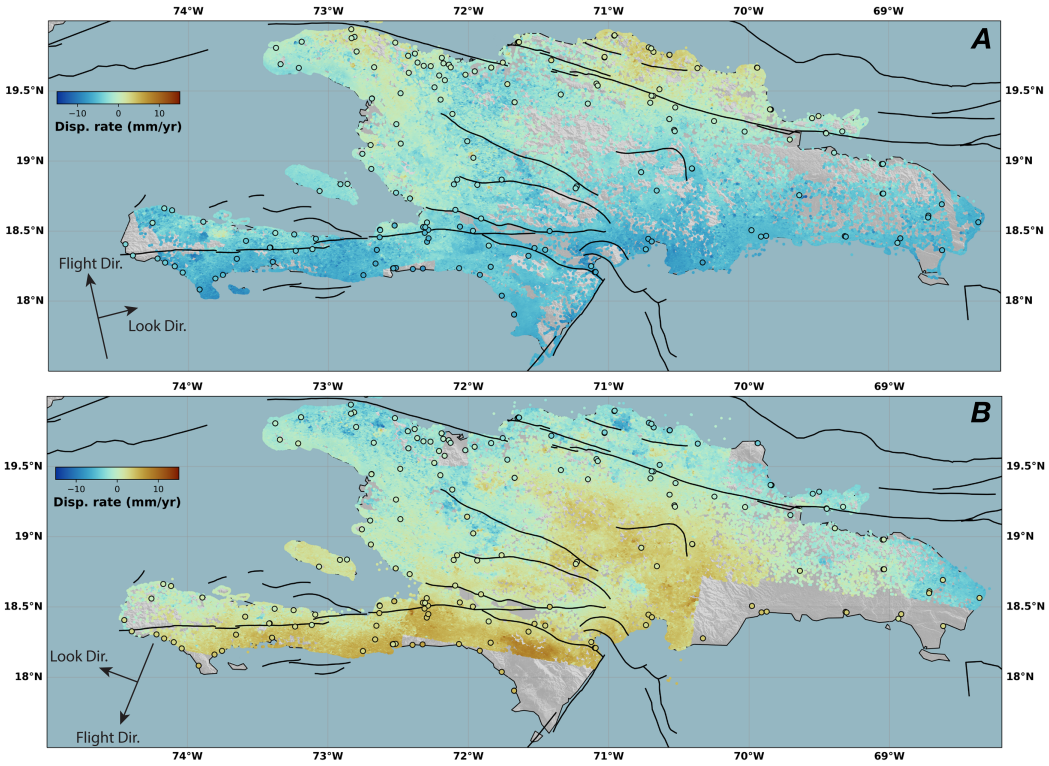

Figure 2. InSAR velocity field over Hispaniola in the LOS direction from the persistent scatterer analysis in the ascending (**Panel A**) and descending (**Panel A**) SAR acquisition geometries (shown by black arrows), after referencing and merging of the three ascending tracks covering the island. Orange, positive values indicate ground motion toward the satellite. Colored dots are GNSS velocities projected onto the ascending LOS for comparison with InSAR velocities. Fault traces are from Saint Fleur et al. (2020).

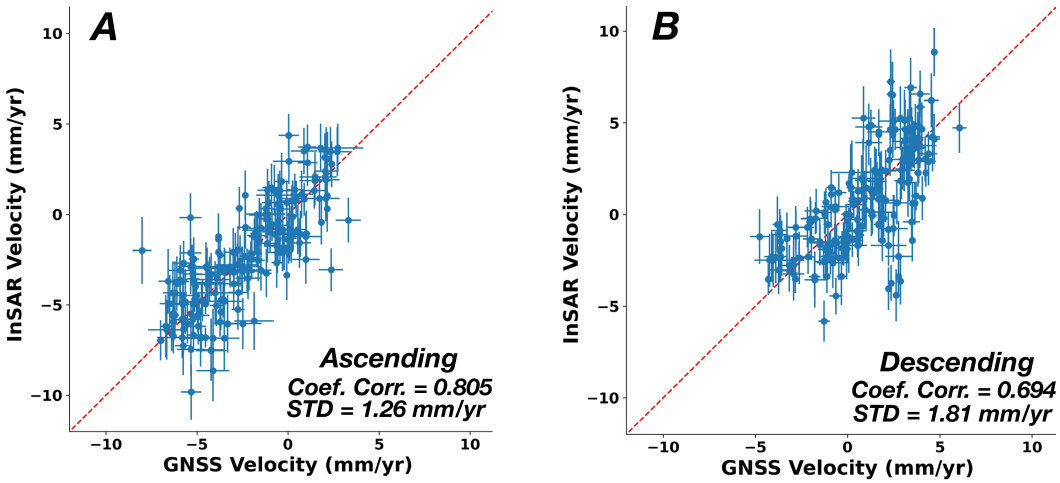

Figure 3. Comparisons between PS-InSAR velocities and GNSS-derived velocities projected onto the ascending line of sight (LOS) in Panel A and the descending LOS in Panel B. In each panel, the reported value corresponds to the standard deviation between the two datasets, and the red dashed line represents the 1:1 identity line.

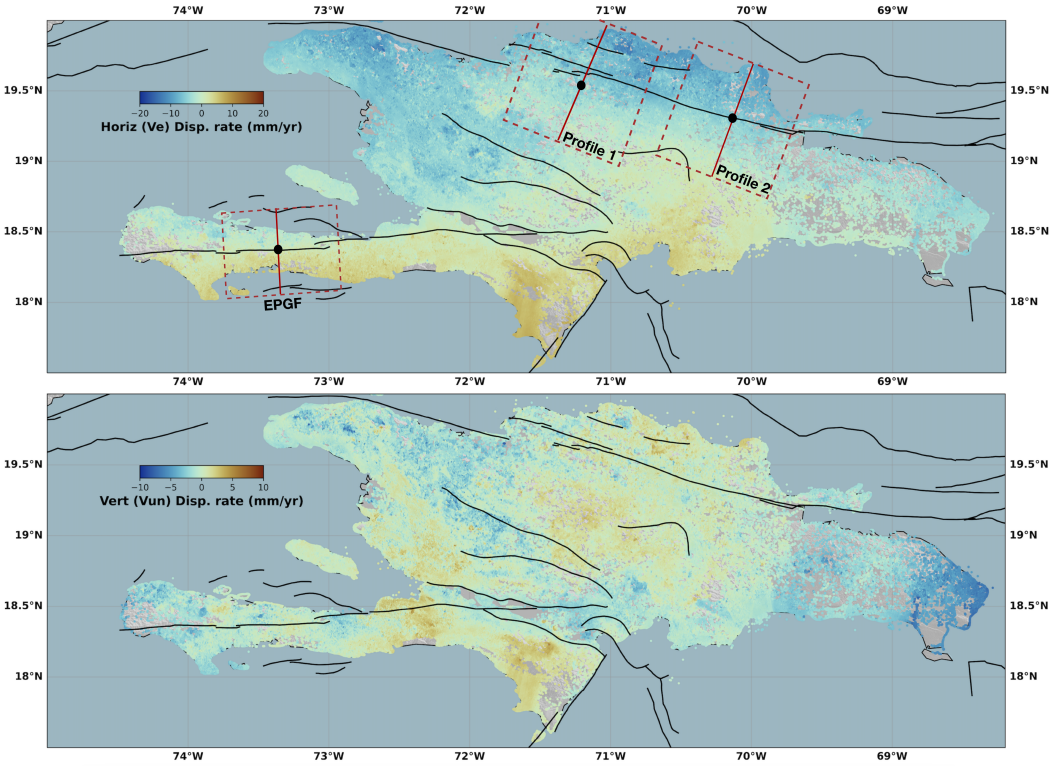

Figure 4. PSInSAR velocities after decomposition of the ascending and descending LOS velocities. Black lines show main fault traces. **Top:** Velocities in the east direction. Red solid lines indicate the locations of the velocity profiles extracted across the Enriquillo–Plantain Garden Fault (EPGF) and the Septentrional Fault. Black dots mark the fault location as estimated from the velocity inversion. Red dashed rectangles outline the swath used to extract the profile data around each fault. **Bottom:** Velocities in the vertical–northward direction.

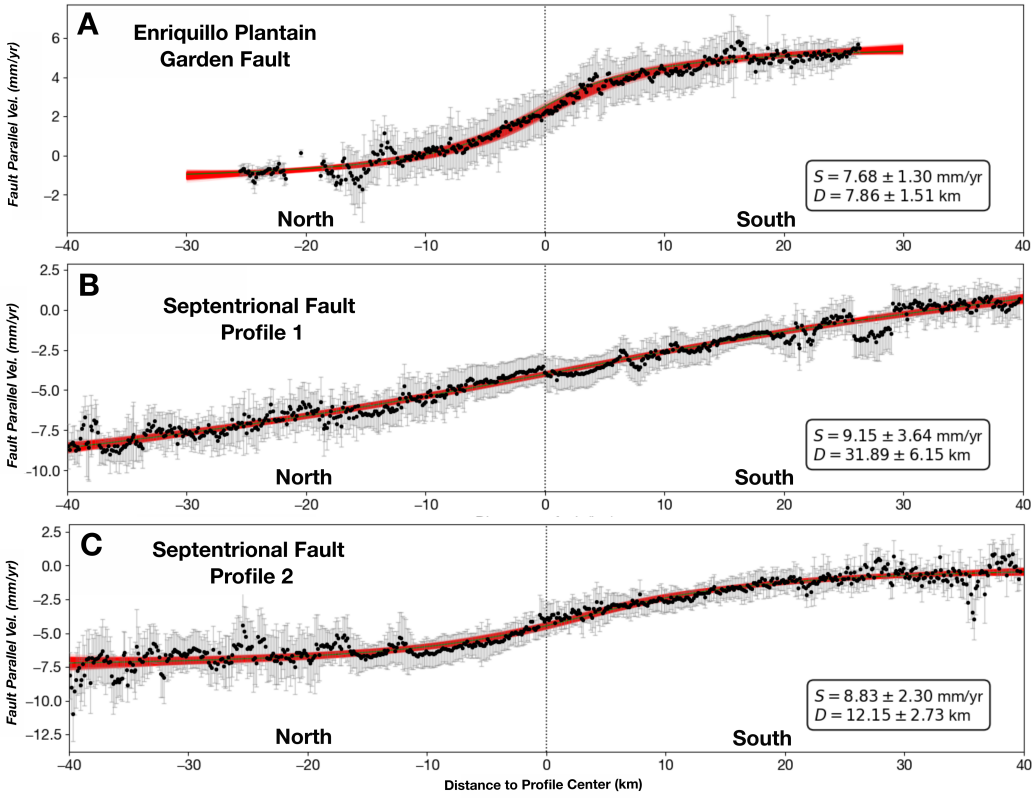

Figure 5. Fault-parallel velocity profiles across the Enriquillo fault (A), Septentrional fault west (B), and Septentrional fault east (C). Profile velocities are computed as the median within 0.6 km bins from the PSInSAR eastward velocities. Zero on the x–axis marks the fault location as estimated from the 1D fault velocity inversion. Black dots and grey error bars show the PSInSAR data and their associated 1-σ uncertainties, dark grey line shows the model mean, red interval shows the model variability from 1,000 realizations drawn from the posterior distribution. Insets report the inferred slip rate S and locking depth D, with uncertainties derived from the posterior sampling (Supplementary Figures S6, S7, and S8).

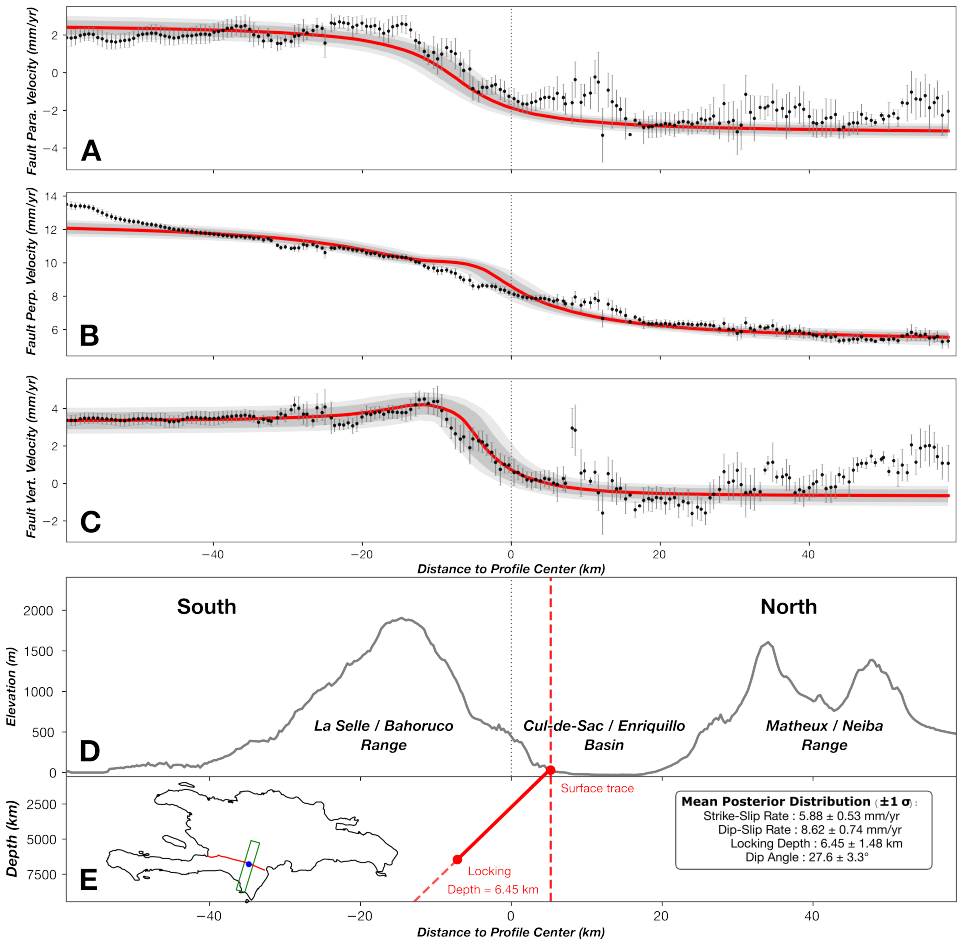

Figure 6. Velocity profiles across the Bahoruco/La Selle range – Enriquillo/Cul-de-Sac basin system. The profile is sampled from the fault-parallel velocity field and its associated uncertainty using gridded data centered at longitude -71.4949deg and latitude 18.3168deg. It is defined with a length of 120 km, a width of 20 km, and an azimuthal orientation of 15°. The resulting profile is then binned along the across-profile distance, with each bin averaged using a mean filter and a bin spacing of 0.6 km. Black dots and grey error bars show the PSInSAR data and their associated uncertainties for the fault-parallel, vertical, and fault-perpendicular velocity components. Red line shows the posterior model prediction from the Bayesian inversion, while the shaded envelopes indicate the associated posterior uncertainty. The lower–right panel shows the posterior estimates for the single-fault model, reported as the posterior mean and associated 1σ uncertainty for the strike-slip rate, dip-slip rate, locking depth, fault-trace position, and fault dip (see also Supplementary Figure S9).

Supporting Information for "Current deformation in Hispaniola from InSAR–derived surface velocities"

B. Raimbault[1,2], R. Jolivet[2,3], E. Calais[2], S. Symithe[4]

[1]Centre National d'Etudes Spatiales, CNES, Toulouse, France
[2]École normale supérieure, Department of Geosciences, Université PSL, CNRS, Paris, France
[3]Institut Universitaire de France, Paris, France
[4]Université d'Etat d'Haïti, Faculté des Sciences, URGéo, Port-au-Prince, Haïti

Content of this file

Figure S1 to S10.

This supplementary file includes figures providing details on the persistent scatterers interferometry data, and figures posterior distributions from the Bayesian fault models.

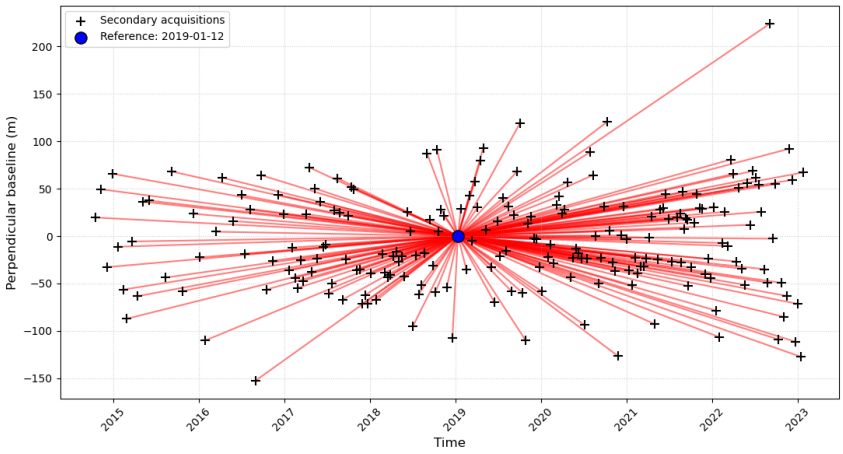
Secondary acquisitions
Reference: 2019-01-12
Perpendicular baseline (m)
Time

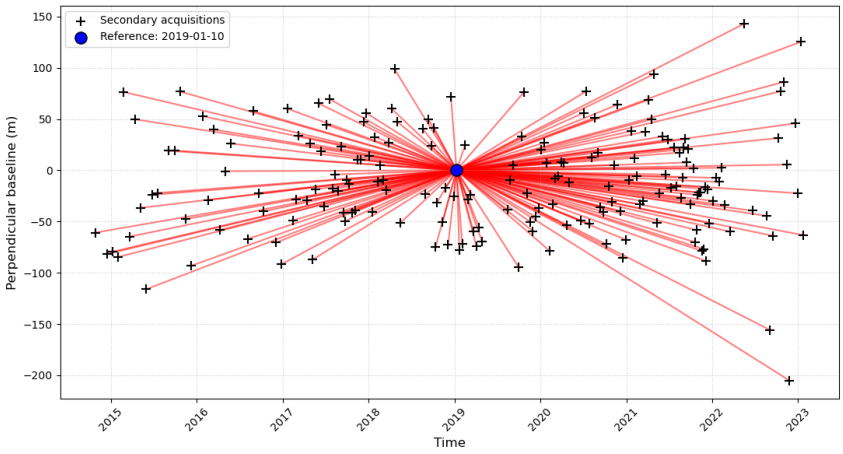
Secondary acquisitions
Reference: 2019-01-10
Perpendicular baseline (m)
Time

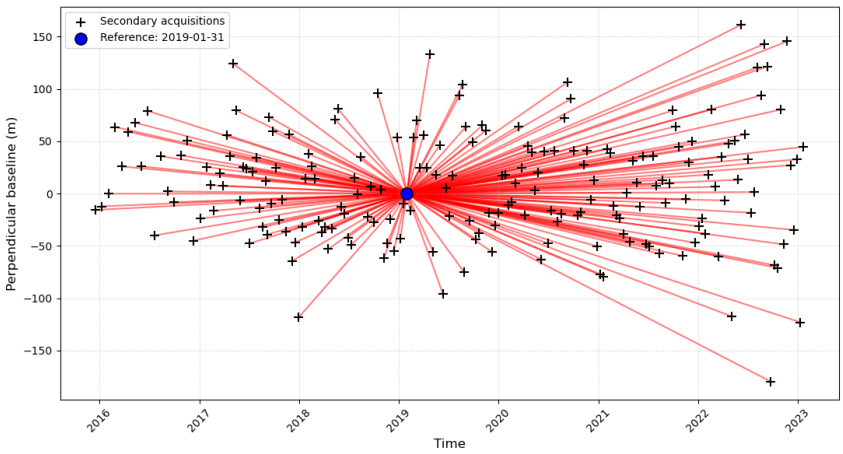
Secondary acquisitions
Reference: 2019-01-31
Perpendicular baseline (m)
Time

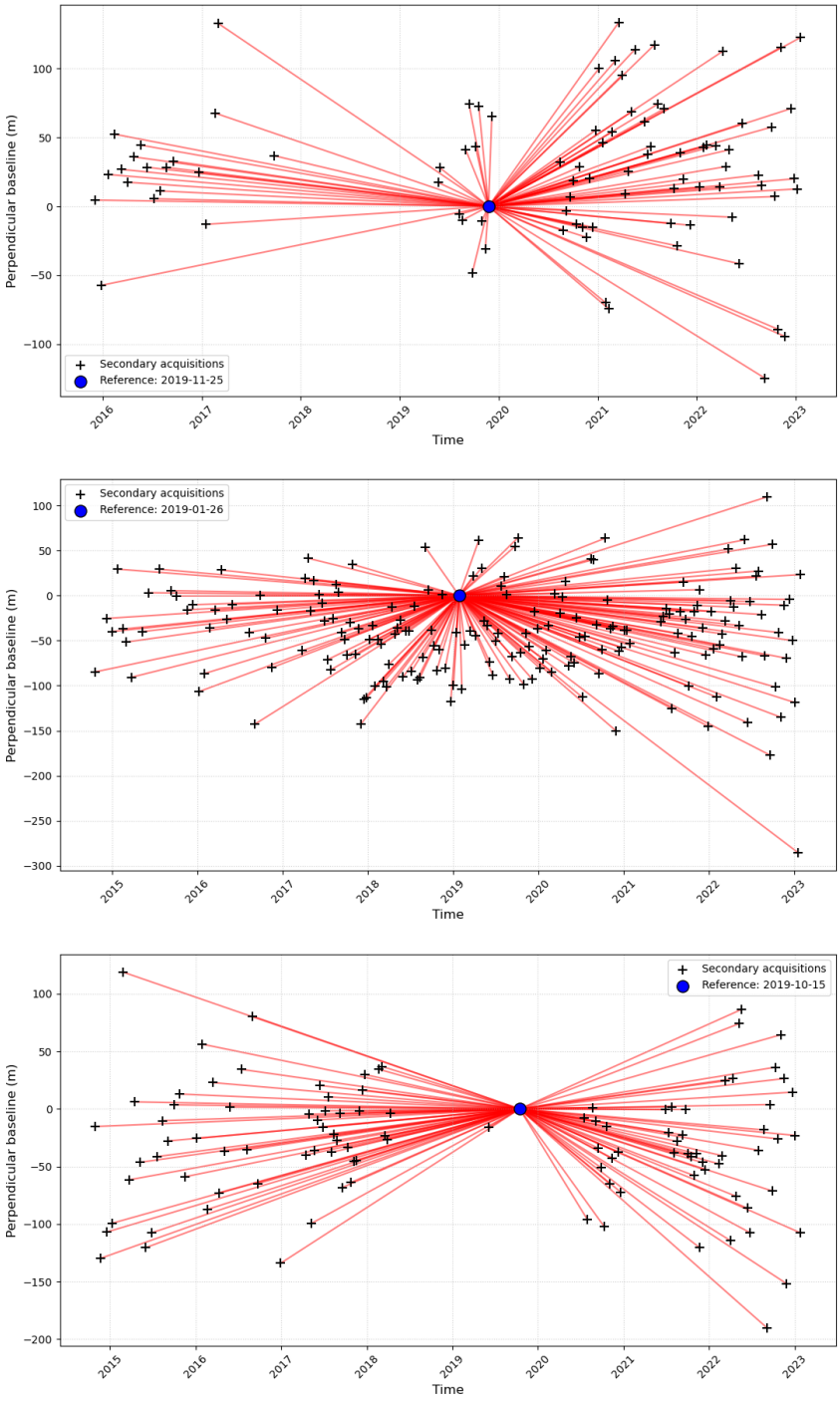

Figure S1. Distribution of perpendicular baselines over time for tracks 4, 142, 106, 69, 33, and 171, in that order from top to bottom. The plot illustrates the interferometric network configuration for the StaMPS Persistent Scatterer (PS) analysis. Each point represents an individual SAR acquisition. The blue circle highlights the reference image, dated 2019-01-12, to which all other secondary acquisitions (black crosses) are co-registered. The red lines represent the interferograms formed, showing the perpendicular baseline (m) relative to the reference as a function of the acquisition time.

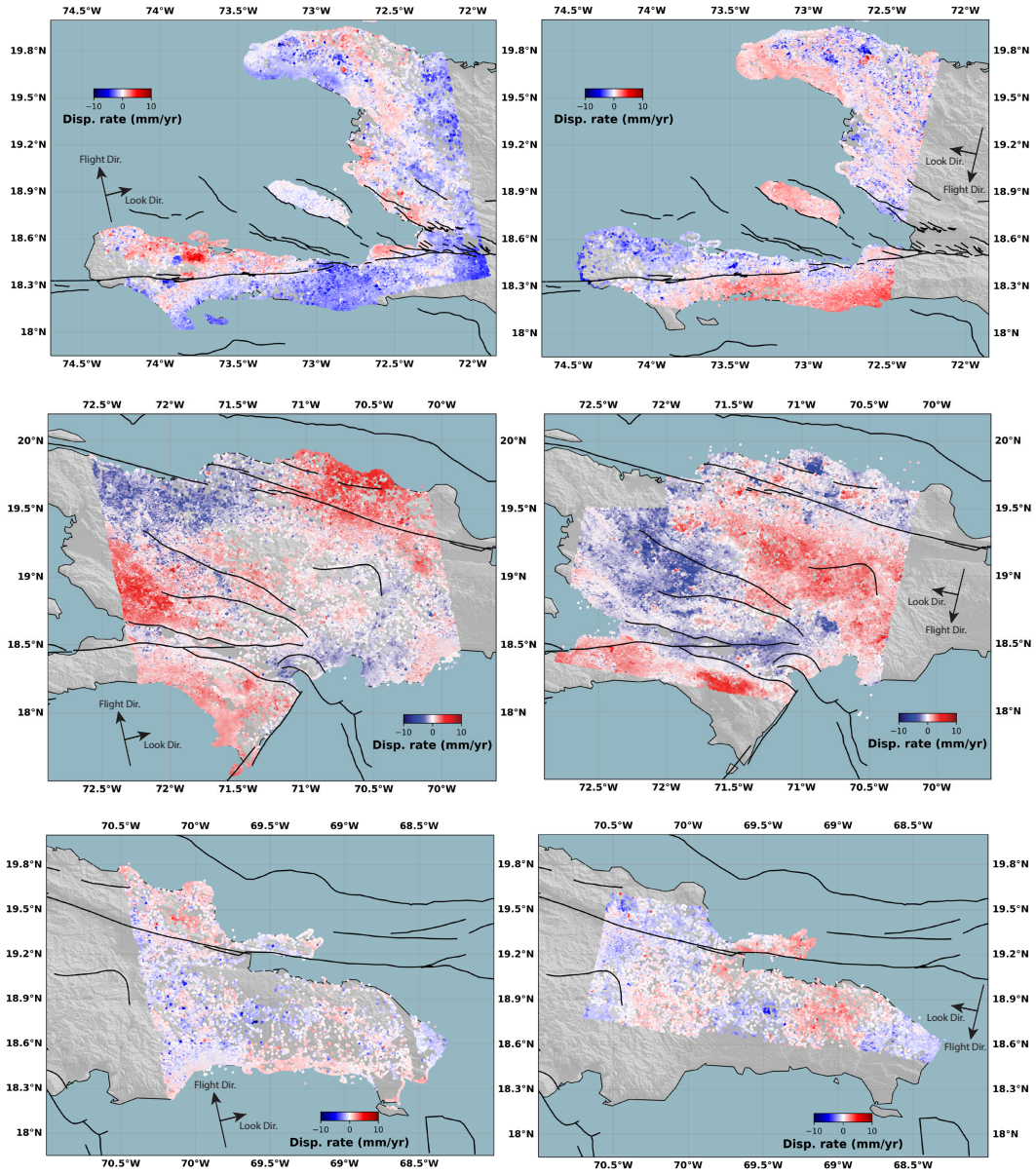

Figure S2. Line-of-Sight (LOS) velocity maps for tracks 4–142, 106–69, and 33–171, in that order from top to bottom. Surface displacement rates, in mm/yr, are derived from StaMPS PS-InSAR processing for the (left) ascending and (right) descending orbits. The color scale ranges from -10 to 10 mm/yr, where blue indicates motion away from the sensor and red indicates motion toward the sensor. Black lines represent major active faults, arrows indicate the satellite flight and look directions for each geometry.

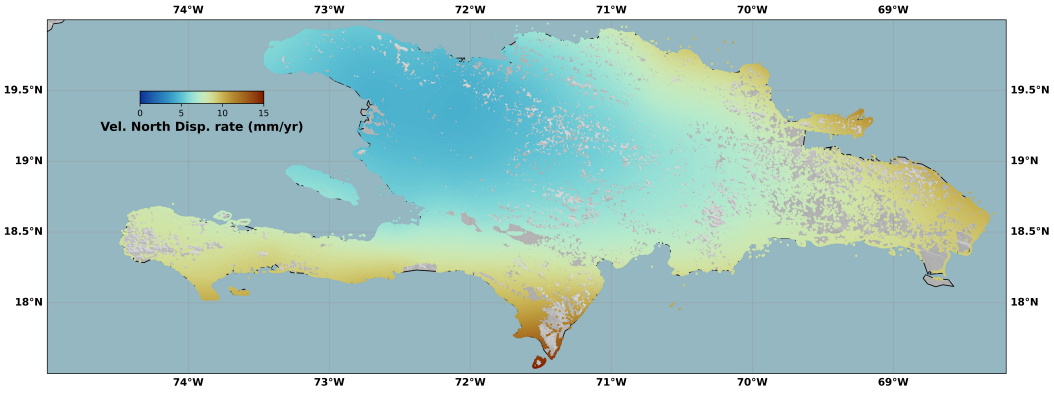

Figure S3. North velocity component at the InSAR positions, obtained by kriging the northward component of the GNSS velocities. The color scale ranges from -10 to 10 mm/yr, with blue indicating motion toward the north and red indicating motion toward the south.

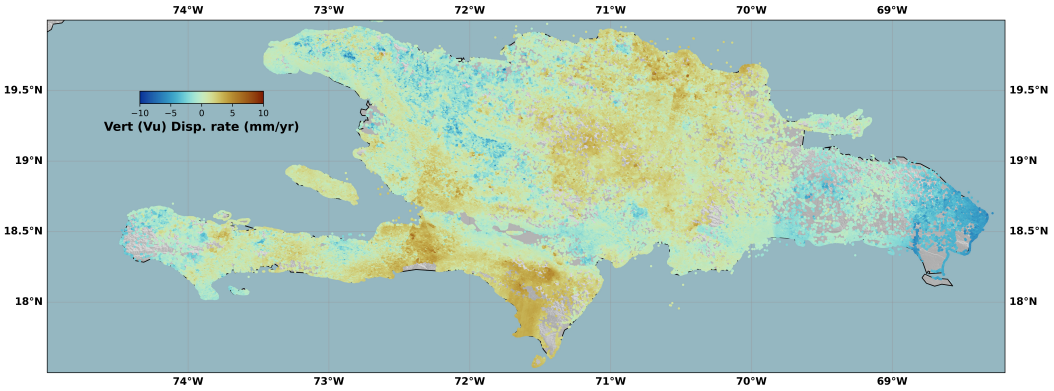

Figure S4. Vertical velocity component at the InSAR positions, obtained by decomposing the V_{UN} InSAR-derived velocities using the kriged V_N velocities (Figure SS3). The color scale ranges from -10 to 10 mm/yr, where blue indicates motion going downward and red indicates motion upward.

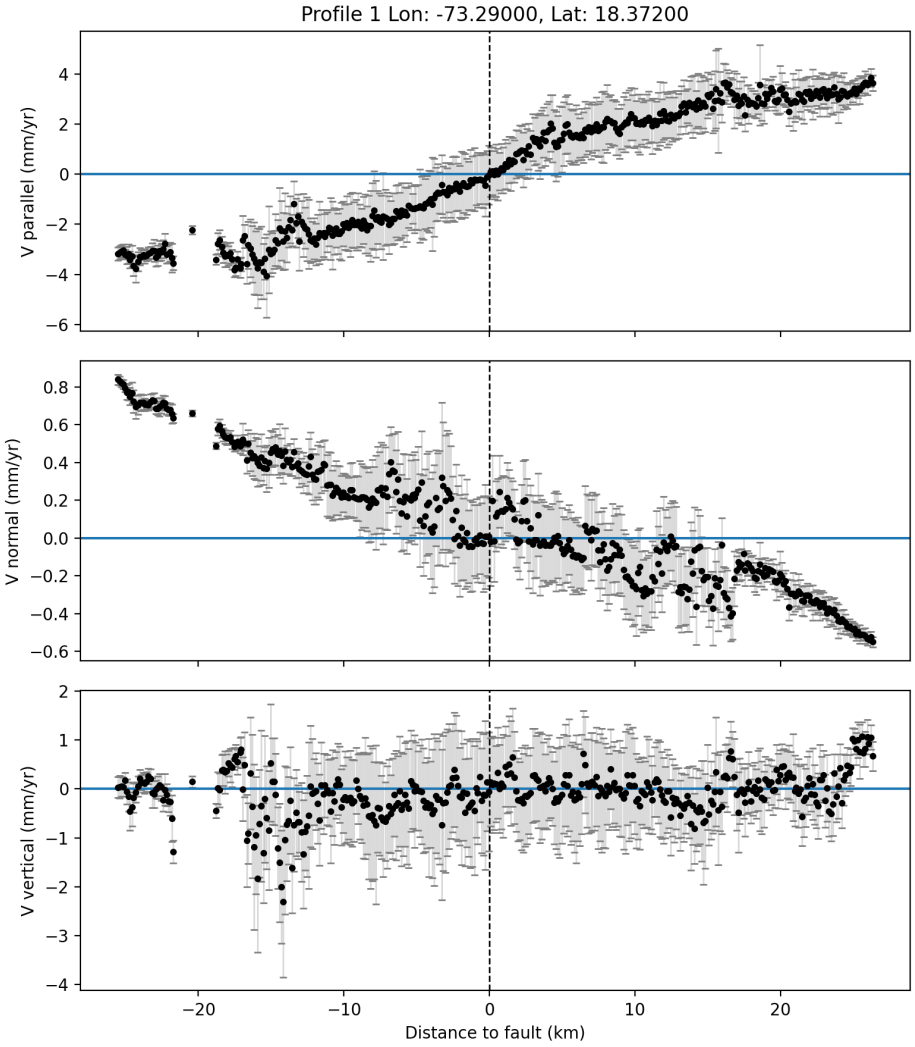

Figure S5. Velocity profiles across the Enriquillo fault showing the fault–parallel (top), fault–normal (middle), and vertical velocities (bottom). Profile velocities are computed as the median within 0.6 km bins from the PSInSAR eastward velocities. Zero on the x–axis marks the fault location as estimated from the 1D fault velocity inversion (see main text). Black dots and grey error bars show the PSInSAR data and their associated 1-σ uncertainties. Note the different y-axis scaling for each component.

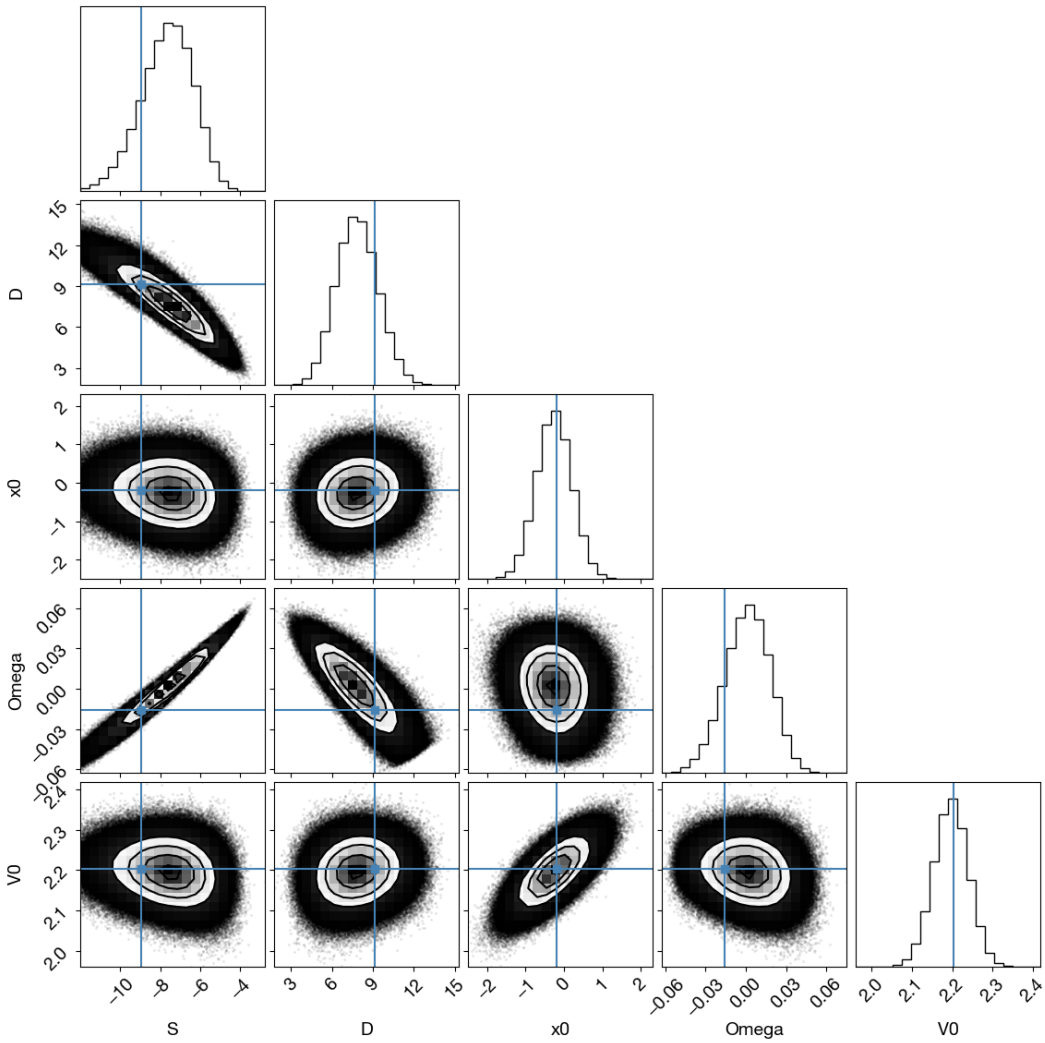

Figure S6. Posterior probability distributions of the 1D screw dislocation Enriquillo fault model parameters obtained from Bayesian sampling of the fault-parallel velocity profile. Diagonal panels show the marginal posterior distributions of each parameter, off-diagonal panels show the joint posterior distributions and parameter correlations. Blue lines indicate the preferred parameter estimates, contours illustrate the main credibility regions of the posterior distributions.

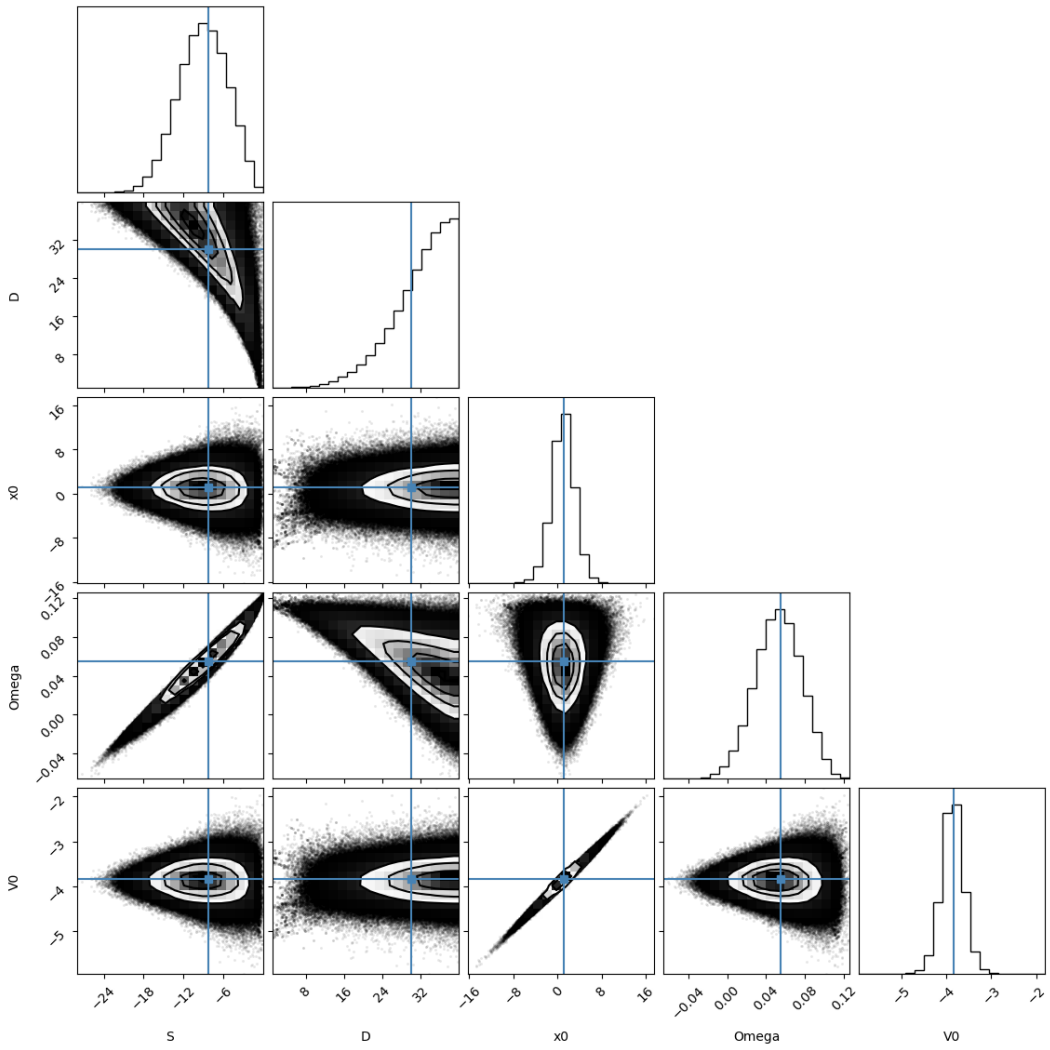

Figure S7. Posterior probability distributions of the 1D screw dislocation Septentrional fault east model parameters obtained from Bayesian sampling of the fault-parallel velocity profile. Diagonal panels show the marginal posterior distributions of each parameter, off-diagonal panels show the joint posterior distributions and parameter correlations. Blue lines indicate the preferred parameter estimates, contours illustrate the main credibility regions of the posterior distributions.

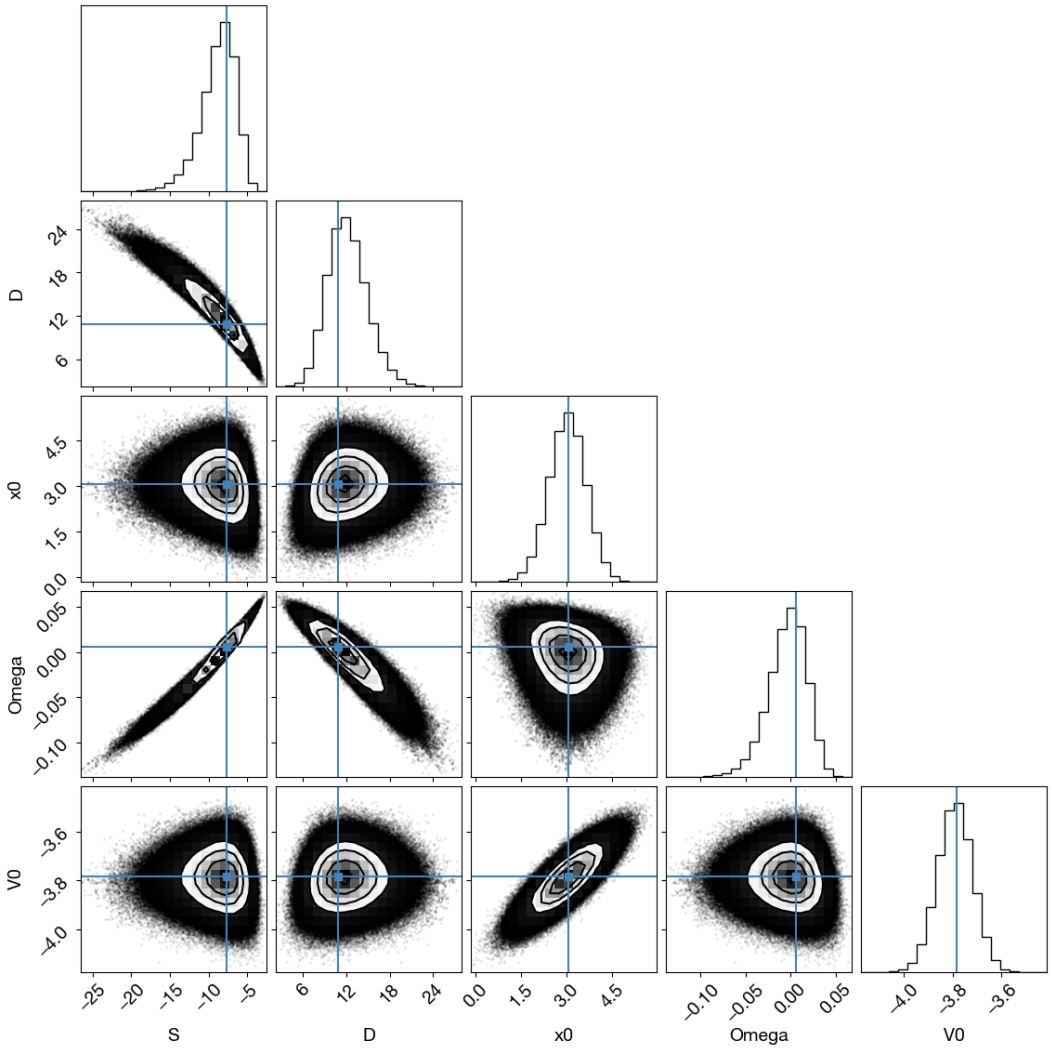

Figure S8. Posterior probability distributions of the 1D screw dislocation Septentrional fault west model parameters obtained from Bayesian sampling of the fault-parallel velocity profile. Diagonal panels show the marginal posterior distributions of each parameter, off-diagonal panels show the joint posterior distributions and parameter correlations. Blue lines indicate the preferred parameter estimates, contours illustrate the main credibility regions of the posterior distributions.

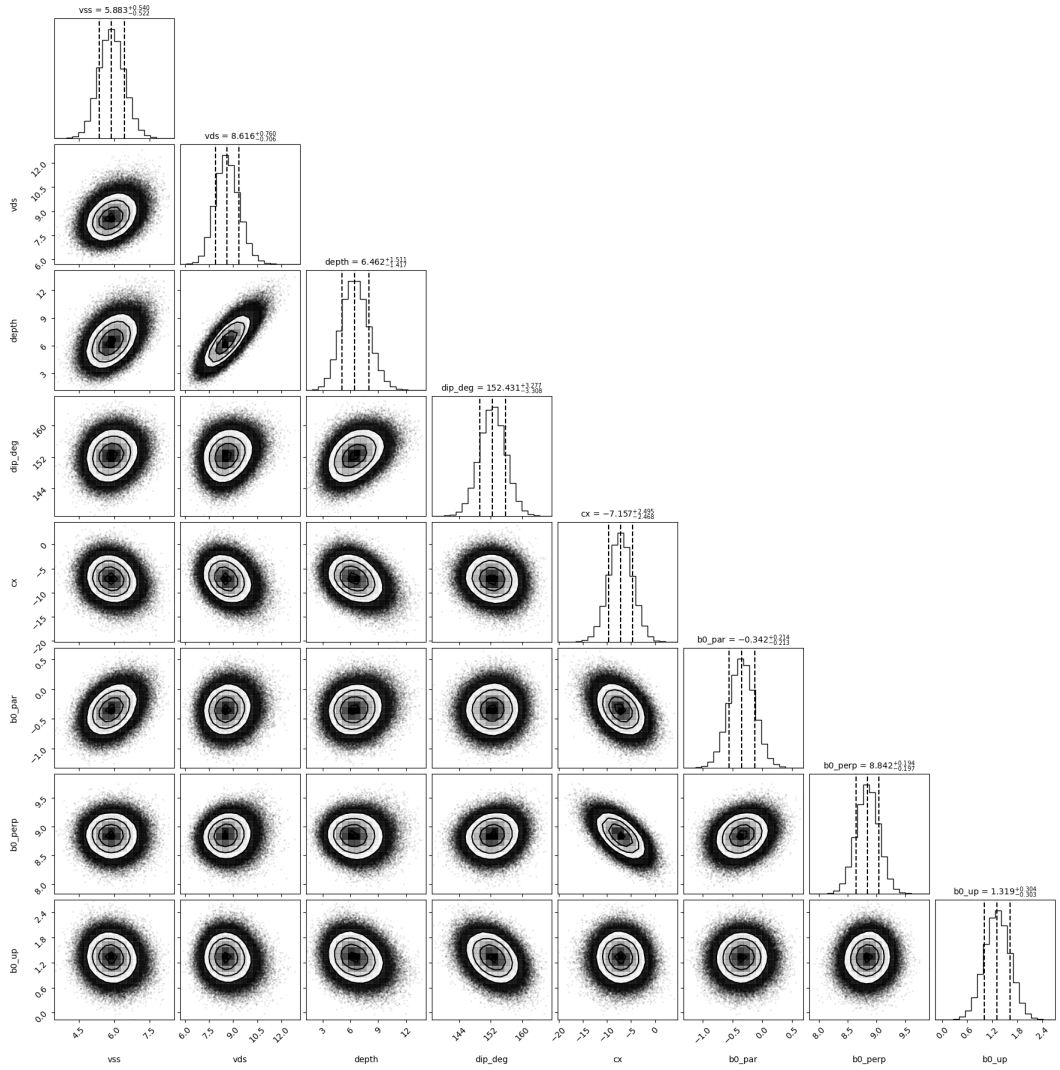

Figure S9. Posterior probability distributions of the 1D screw dislocation Jérémie–Malpasse fault west model parameters obtained from Bayesian sampling of the three-component velocity profile. Diagonal panels show the marginal posterior distributions of each parameter, off-diagonal panels show the joint posterior distributions and parameter correlations. Blue lines indicate the preferred parameter estimates, contours illustrate the main credibility regions of the posterior distributions. The inverted parameters are the strike-slip rate V_{ss}, dip-slip rate V_{ds}, locking depth D, fault dip δ, horizontal fault position c_x, and constant velocity offsets for the fault-parallel, fault-normal, and vertical components.

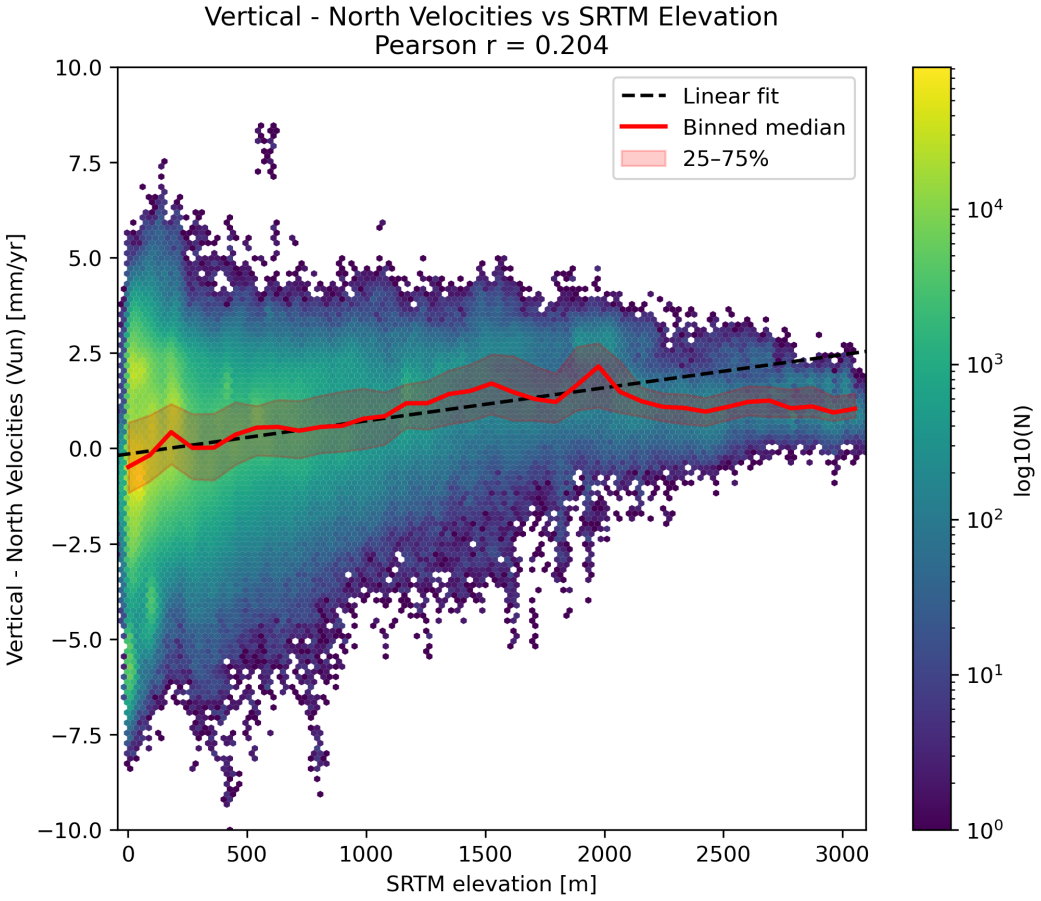

Figure S10. Relationship between the V_{Un} velocity component and SRTM elevation. The point density is shown in logarithmic scale, with warmer colors indicating a larger number of observations. The black dashed line shows the linear fit to the data, while the red curve shows the binned median velocity as a function of elevation. The shaded red envelope indicates the interquartile range between the 25th and 75th percentiles within each elevation bin. The Pearson correlation coefficient is indicated above the panel.